Heat transfer enhancement on CSP tubular receivers using partially filled Raschig Ring porous inserts: A numerical study

Original
Heat transfer enhancement on CSP tubular receivers using partially filled Raschig Ring porous inserts: A numerical study / Ebadi, Hossein; Cammi, Antonio; Fathi, Nima; Savoldi, Laura. - In: SOLAR ENERGY. - ISSN 0038-092X. - 297:(2025). [10.1016/j.solener.2025.113635]

Publisher:
Elsevier

Published
DOI:10.1016/j.solener.2025.113635

Solar Energy 297 (2025) 113635

Contents lists available at ScienceDirect

Solar Energy

journal homepage: www.elsevier.com/locate/solener

Heat transfer enhancement on CSP tubular receivers using partially filled Raschig Ring porous inserts: A numerical study

Hossein Ebadi [a,*], Antonio Cammi [b,c], Nima Fathi [d,e], Laura Savoldi [a]

[a] MAHTEP Group, Dipartimento Energia "Galileo Ferraris" (DENERG), Politecnico di Torino, Turin, Italy
[b] Emirates Nuclear Technology Center (ENTC), Department of Mechanical and Nuclear Engineering, Khalifa University, Abu Dhabi 127788, United Arab Emirates
[c] Department of Energy, Politecnico di Milano, Milan 20133, Italy
[d] Mechanical Engineering Department, Texas A&M University, College Station, TX, USA
[e] Department of Marine Engineering Technology, Texas A&M University, Galveston, TX, USA

ARTICLE INFO

Keywords:
CSP
Flow insert
Porous media
Partial filling
Heat transfer enhancement

ABSTRACT

This study presents a computational investigation to evaluate and analyze the performance of partially filled porous inserts, composed of metallic Raschig Rings in gaseous concentrated solar power absorbers. Two filling configurations, Lateral Filling (placing inserts along the tube sides) and Central Filling (positioning them along the central axis), were analyzed with different designs. Comparison was conducted by varying filling indices to balance thermal enhancement and pressure drop reduction. The fluid dynamics, encompassing flow velocity, pressure, and temperature gradients were meticulously studied using validated 3D pore-scale computational fluid dynamics models. These models were successfully able to capture the transitional behavior of the fluid between porous and clear regions. The results reveal similar flow leakage trends in both configurations with notable variations along the porous medium. The two designs exhibited unique heat transfer mechanisms, resulting in different temperature profiles on the absorber wall. Partial Filling significantly reduced the pressure drop – a major limitation of fully filled designs –by up to 95%, while simultaneously enhancing the overall absorber performance. This study demonstrated that the partially filled design could achieve up to 40% higher energy efficiency and nearly 90% greater exergy efficiency compared to simple tube designs, offering an alternative for solar high-temperature systems.

1. Introduction

In CSP technologies, molten salt is the most commonly used heat transfer fluid (HTF), capable of operating at temperatures up to 565 °C. However, to achieve the higher temperatures 700 °C or more required for next-generation systems, a new HTF is needed due to the inherent limitations of molten salts [1]. Among the alternatives, air has emerged as a promising candidate due to its numerous advantages, such as reduced capital and operational costs, simplified system design, and lower infrastructure requirements. Furthermore, air is environmentally friendly, being non-toxic and non-corrosive, while conserving resources by eliminating the need for extensive water use in cooling systems. Despite these benefits, the primary challenge lies in air's lower heat transfer capacity compared to molten salts and thermal oils.

To address this limitation, researchers have explored various thermal enhancement techniques. For instance, turbulators can effectively improve fluid mixing within receiver channels [2]. Additionally, porous structures have been proposed to enhance fluid-wall heat transfer, especially in tubular CSP receivers [3]. While CSP linear focusing absorbers have been widely integrated with the flow inserts, point-focusing systems have received considerably less research attention. In this regard, Hazmoune et al. [4] conducted a 3D CFD study to analyse a solar tower tubular absorber with helical fins. Moreover, Hatcher et al. [5] proposed a multiphasic investigation to study hydro-thermal–mechanical performance of tubular absorbers with different internal fins under the solar radiation in a solar tower. Haddad et al. [6] used several 3D printed tubes, enhanced with internal fins and tested them in a furnace heater, simulating solar heat flux. In another study [7], it was found that combination of fins with a double-pass absorber tube improves the Nu by 50 % for an air-based solar tower system.

Among these techniques, the integration of porous inserts has gained significant attention due to their ability to improve thermal properties, such as enhancing convective heat transfer coefficients and increasing

---

* Corresponding author.
E-mail address: hossein.ebadi@polito.it (H. Ebadi).

https://doi.org/10.1016/j.solener.2025.113635
Received 29 January 2025; Received in revised form 15 May 2025; Accepted 23 May 2025

Nomenclature

Abbreviations

CF	Central Filling
CFD	Computational Fluid Dynamic
CSP	Concentrating Solar Power
DEM	Discrete Element Method
FP	Full Porous
HTF	Heat Transfer Fluid
LF	*Lateral Filling*
LTE	*Local Thermal Equilibrium*
LTNE	*Local Thermal Nonequilibrium*
PEC	Performance Evaluation Criterion
PF	Partial Filling
PFI	Partial Filling Index
PIV	*Particle Image Velocimetry*
PSA	Plataforma Solar de Almeria
PTC	Parabolic Trough Collector
RANS	Reynolds-Averaged Navier-Stokes
RR	Raschig Ring
SP	Smooth Pipe
TC	Thermocouple
TPMS	Triply Periodic Minimum Surface

Greek symbols

α	absorption
β	viscous resistance coefficient (m^{-2})
Δp	pressure drop (Pa)
ϵ	emissivity
θ	incident angle
κ	turbulent kinetic energy (m^2/s^2)
μ	dynamic viscosity (Pa.s)
ρ	fluid density (kg/m^3)
η	efficiency
σ	Stefan–Boltzmann constant
σx	standard deviations in x direction
σy	standard deviations in y direction
φ	solar flux (W/m2)
ω	specific dissipation rate of the turbulent kinetic energy (s^{-1})

Symbols

Cp	specific heat capacity (J/kg/K)
D	diameter (m)
E	energy flux (W/m^2)
E_x	exergy flux (W/m^2)
ETC	Effective Thermal Conductivity (W/m/K)
f	friction factor
HTC	heat transfer coefficient (W/m^2/K)
h	porous insert height (m)
k	thermal conductivity (W/m/K)
L	tube length (m)
m	mass flow rate (kg/s)
N	cell number
Nu	Nusselt number
p	pressure (Pa)
Q	Airflow rate (L/min)
Re	Reynolds number
S	surface area (m^2)
T	temperature (K)
U_L	Heat loss coefficient (W/m^{2}K)
V	total volume of the model (m^3)
v	velocity magnitude (m/s)
W_P	pumping work demand (W)
Z	Porous insert length (m)
x, y, z	coordinate system

Subscripts

a	air
amb	ambient
abs	absorbed
ave	average
c	cross section
con	Concentrated solar flux on the tube
conv	convection
des	Destruction
Dish	parabolic dish
eff	effective
el	electrical
en	energy
Ex	exergy
ext	external
f	fluid
fm	fluid mean
focus	focused solar flux at the test table
fr	friction
g	glass envelope
hot	hotspot
i	inlet
int	internal
l	loss
m	mean
o	outlet
opt	optical
ovr	overall
p	pipe
peak	peak flux
rad	radiation
S	solar
sky	sky
Sun	sun
th	thermal
u	useful
w	wind

the overall heat transfer coefficient [8]. However, a major drawback of porous inserts is the accompanying pressure drop, which can lead to higher pumping power requirements and increased operating costs. To mitigate this issue, Partial Filling (PF) configurations have been introduced. PF configurations strategically position porous materials within the channel to reduce flow resistance in clear regions, thereby minimizing pressure drops while maintaining enhanced heat transfer performance [9]. This approach is particularly relevant for solar air heaters, a sustainable energy technology that benefits significantly from heat transfer enhancements due to air's inherently low thermal conductivity.

Several studies have demonstrated the effectiveness of PF porous inserts in solar air heaters. For example, Al-Nimr and Alkam [10] achieved up to a 30 % increase in thermal efficiency by inserting a porous substrate near the absorber plate. Fallah Jouybari and Lundstrom [11] demonstrated a six-fold improvement in the Nusselt number by incorporating a thin layer of porous material, though it doubled the pressure drop. Similarly, Singh [12] revealed that a 25 % fractional porous interface with 0.93 porosity in a wavy channel solar air heater improved heat transfer eightfold at the cost of an 84-fold increase in the friction factor.

While the potential of PF porous inserts for high-temperature solar air heaters remains underexplored, several studies have investigated their application in other thermal systems. For example, Zheng et al. [3] evaluated PF configurations in CSP absorbers using mixed nitrate molten salts, achieving superior heat transfer performance compared to full porous (FP) configurations. Similar success has been observed with other fluids and porous materials in Parabolic Trough Collectors (PTCs) [13], with reported improvements in thermal efficiency and entropy reduction using CFD analysis.

The position of porous insert within the channels is another critical factor impacting thermal enhancement. Yang et al. [14] demonstrated that placing the porous medium in the core region improves heat transfer by redirecting fluid particles closer to the wall. Jouybari et al. [15] numerically demonstrated that the thermal conductivity of the porous media has a greater influence on the variation of the Nusselt number in the boundary configuration than in the central arrangement. Other studies, such as those by Akbarzadeh et al. [16] and Ahmed et al. [17], showed the importance of optimizing the position of the porous material to balance heat transfer and pressure drop effects.

In the optimization of PF porous inserts for various thermal applications, the methodology used to study the complex fluidic behaviors at flow-porous interfaces is crucial for understanding the heat transfer mechanisms within these designs. To elaborate on this topic, Anuar et al. [18] conducted an experimental attempt, using Particle Image Velocimetry (PIV) and thermal image methods to visualize the fluid dynamics of a channel partially filled with a metal foam block at different heights and pore density. During the experiments, it was observed that although a fraction of the flow goes into the porous region, the flow has the tendency to leave into the free stream region after a certain foam length, depending on the pore density. Nazari et al. [19] employed the lattice Boltzmann method to show that the topology of the flow and heat transfer of 2D channel with PF porous foam relies strongly on the porous arrangement, blockage ratios (the ratio of obstacles blockage area to channel cross-sectional area), Re number and porosity. Alihosseini and Jafari [20] implemented a pore scale study to investigate a one-side heated tube under an unsteady–state CFD model with constant wall temperature using FP, and 3 PF configurations of aluminum foam and Al_2O_3/ water-based nanofuid. Li and Hu [21] studied the forced convection heat transfer inside a pipe partially filled with porous media located at two inner walls, using local thermal nonequilibrium (LTNE) conditions. Results indicated that under a constant heat flux, the hollow ratio (the diameter of the empty space/ the diameter of the pipe) has a special role in achieving the optimum Nu number. Forooghi et al. [22], suggested that in simulating a PF channel when the thermal conductivity ratio is high, the LTNE model must be used in the energy equations for both solid and fluid phases in the porous medium. However, when the Darcy number decreases, LTE could provide some reasonable results. Lisboa et al. [23] found that in the case of PF channels, the LTNE hypothesis is a good approximation for the whole cross-section of the channel, except at the interface between the free fluid and the porous medium.

In the presented literature review, most of the numerical works are treated with a porous medium (macro model) approach, using special momentum and energy equations for the porous zone, while the rest of the fluid domain is modeled with fundamental equations. Although the reported findings provided some insights into the fluid flow and heat transfer problems in PF porous media integrations, some challenges such as the flow leakage from the porous to non-porous regions and the mechanism of energy and momentum transportation across the interface still remain unknown and require a pore-scale (micro) modeling for further clarification [26].

This study concentrates on a novel porous medium composed of small metallic Raschig Rings (RR), which has already been used as porous media in solar receivers through experimental and numerical studies [24–26], showing significant thermal enhancements. The increase in energy and exergy efficiencies (up to 50 and 75 %, respectively) was proven experimentally by testing in a solar furnace tubular CSP receivers with FP RR inserts [27]. A numerical model was developed at the pore-scale and verified against the experimental results, confirming the effects of RR porous inserts on improving the heat transfer rate up to 15 times and increasing the pressure drop by 450 times, if compared to a simple receiver design [28].

As metallic (copper) RRs have proven to be very effective in increasing the receiver performance, here we address their use as PF inserts, to maintain the enhanced heat transfer and minimize fluid dynamics (pressure losses), to advance this technology further for CSP air heaters. To achieve the most efficient design under the studied working conditions, a thorough numerical investigation was conducted on a solar receiver tube equipped with various PF and FP RR inserts. This study considers a 3D pore-scale simulation of the proposed solar absorbers to address deeply for the first time the fluidic and thermal features of various PF porous inserts, under non-uniform concentrated solar radiation. Moreover, the instantaneous comparison between the proposed porous inserts in the central (at the fluid core zone) and lateral (attached to the heated side) designs was unexplored in the pore-scale simulation. One of the important aspects, which is less addressed in the literature and still needs attention, is the study of flow behaviors at the interface between the porous and non-porous regions, imposing the real working conditions such as the heat flux, and fluid mass flow rates. The findings from this study are highly valuable for designers and researchers in this field, offering crucial guidelines for incorporating any type of porous media in PF formats with CSP tubular absorbers.

2. Physical and numerical models

2.1. Receiver concept and design

The use of porous media in solar absorbers has gained attention for its ability to address the dual challenge of maximizing heat transfer efficiency and maintaining system durability under high thermal loads. Innovative configurations such as RR porous inserts have been developed to harness concentrated solar energy effectively, leveraging their unique geometric and thermal properties. These inserts are particularly suited for tubular absorbers where efficient heat distribution is critical to system performance and longevity. Fig. 1a illustrates the concept of the FP RR insert in a tubular absorber. This design involves brazing a porous block of RRs inside the tube to enhance heat transfer, as detailed in [27]. The structure of the porous medium was formed using a number of RR made of copper, coated with a gold alloy and brazed together with a porosity of 78.8 %, the same material used in previous works [27,28]. During the manufacturing phase, rings form a packed structure inside the tube with a desired configuration. Then, a brazing material is applied to the RRs, which after the curing time becomes a united porous medium with solid attachment to the interior of the sample. The RR porous medium was positioned at the focal area where the Gaussian-shaped flux peak forms, to exploit the highest available thermal energy for air heating purposes.

Based on the encouraging experimental results of the receivers with FP integration, two sets of PF configurations were selected based on the literature as shown in Fig. 1b. The Lateral Filling (LF) design is used to explore the effects of the RR in extending the heat transfer area and promoting the heat flow from the heated wall. On the other hand, the Central Filling (CF) design considers inducing turbulence, and improving fluid distribution in the fluid core area for better convective heat transfer between the solid and fluid. It should be noted that the CF inserts are supposed to be placed in the centre by a connecting rod, which is not shown and not considered in this study. A smooth pipe (SP) and a FP model are also included among the options here, to provide a comprehensive comparison over various designs, operating under four levels of airflow as $Q_1 = 750$ NL/min (16 g/s), $Q_2 = 1000$ NL/min (21 g/

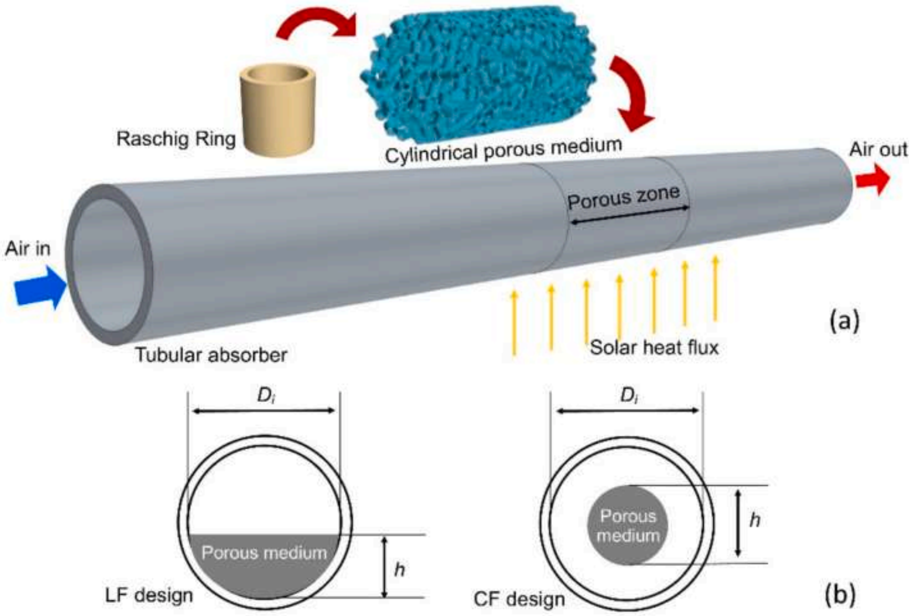

Fig. 1. RR porous integration with tubular absorbers in tubular solar absorbers; (a) schematic of FP integration [27], (b) schematic of the two PF concepts.

s), $Q_3 = 1250$ NL/min (27 g/s), and $Q_4 = 1500$ NL/min (32 g/s), where N denotes normal conditions at $T = 0$ ∘C and $p = 1$ bar. The chosen rate range ensures that, given the applied heat flux, the minimum rate needed to keep the tube's temperature below its softening point is maintained. This selection is crucial for avoiding structural damage and maintaining the integrity of the system while using a simple design. In this study, a parametric factor named Partial Filling Index (*PFI*) (Eq. (1) was defined to test various PF porous insert configurations in the same solar absorber, as reported in Table 1.

$$PFI = \frac{h}{D_i} \tag{1}$$

In eq. (1), h is the height of the porous block in the case of LF designs and is the diameter of the porous block in the case of CF designs, while D_i is the inner diameter of absorber tube (see Fig. 1b).

Non-uniform and one-sided heating with a constant solar peak flux of 0.4 MW/m^2, as an average standard value comparable to solar furnaces, was used to explore the linkage between thermal enhancement and friction factor increments within each design. Tube and porous length were selected based on the experimental work [27] conducted at the Solar Furnace (SF60) located at Plataforma Solar de Almeria (PSA), Spain during the summer of 2022. Although based on the optical characteristics of SF60, a total area of 12 × 12 cm^2 is needed to capture the entire concentrated flux, the reference studies [2,25,29] focused only on a tube located horizontally at the centre of heat flux. Table 2 provides the details of the experimental parameters and test facility extracted from the reference case [29].

2.2. *Numerical models*

The numerical work for this study comprises two interconnected phases. First, a transient Discrete Element Method (DEM) model was employed to create the RR geometries. Next, a thermal model was developed, to simulate variable hydraulic and thermal conditions inside the samples.

2.2.1. *Development of porous media structure*

To model the RR particles, a time-dependent discrete element model was used to model the falling of RR particles into a control volume under the influence of gravity. A Lagrangian multiphase model was implemented where, in the multiphase interaction, the DEM phase interaction was set as the cylinder for both the first and second phase and a linear spring model with a constant stiffness of 10000.0 N/m was used. The void space between the DEM particles was considered as air with 0 velocity and 0 reference pressure. The simulations were conducted in a laminar regime, covering a total physical time of 10 s with a time step of 0.001 s. The generation of the RR porous medium began by defining the volume of the bed and then running the DEM simulation. At each step, a certain number of solid cylindrical particles were injected. The particles were randomly injected in a specific number based on the desired target porosity, with angular and axial velocities both set to 0. The procedure continued until the required number of particles was achieved, and they settled in the bed. Finally, by extracting the position of each particle, the solid cylinders were replaced by hollow cylinders to create the actual porous geometry with RR as the particle component. Fig. 2 illustrates the process of generating the FP model using the DEM method. As a result, the solid region was made by combining the RR porous matrix with the absorber tube, in which a two-segmented field function was applied to define a temperature-dependent thermal conductivity for the tube and a constant effective value of 500 W/m/K for the RR porous zone [28]. The fluid domain was formed by subtracting the RR porous matrix from the internal part of the tube and a contact interface was assigned between the fluid and solid regions to transfer hydraulic and energy characteristics from one domain to another.

2.2.2. *Development of physical and thermal model*

A numerical 3D steady-state conjugate heat-transfer model was developed using the Simcenter STAR-CCM+ software. The simulation accounted for convection and radiation losses under one-sided non-uniform solar heating. The CFD simulations were conducted using a segregated flow solver to resolve the momentum coupled with a segregated energy solver for temperature distribution. Under-relaxation factors of 0.3 for pressure, 0.7 for velocity, 0.99 for energy-solid and 0.9 for energy-fluid were applied to ensure numerical stability and facilitate convergence. Moreover, convergence was considered when the residuals of all governing equations dropped below 10^{-5}, with all residuals exhibiting smooth and monotonic decay, indicating numerical stability and solution reliability.

The fluid domain was also extended by 200 mm upstream, respecting L/D_i 10 before the porous region to ensure the flow develops completely

Table 1
Various porous geometries used in this study.

Case ID	PFI	3D model	Case ID	PFI	3D model
SP	–		CF25	25 %	
LF25	25 %		CF50	50 %	
LF50	50 %		CF75	75 %	
LF75	75 %		FP	100 %	

Table 2
Parameters of the experimental test facility and parameters used in CFD model development.

Parameter	Symbol	Value/Dimension
Tube wall thickness	–	2.5 mm
Tube inner diameter	D_i	21 mm
Tube length	L	250 mm
Porous length	Z	40 mm
Tube material	–	316L stainless-steel
Solar peak flux	φ_{peak}	0.4 MW/m^2
Tube coating	–	PYROMARK 2500
Tube absorptivity	α	0.95
Airflow rate	Q	750, 1000, 1250, 1500 NL/min
Air inlet temperature	T_i	300 K
Reference pressure	p_{ref}	10 bar

before it approaches the porous section. As far as the boundary conditions are concerned, a velocity inlet interface was defined on the internal fluid domain, while a pressure outlet ($p = 0$) condition was set for the outlet face. The concentrated solar flux was simulated through user-defined field functions applied to the irradiated side of the sample (Fig. 3).

The thermal analysis in this work was performed using a segregated flow temperature model and the following assumptions were made for the simulations:

- The solid and fluid properties are temperature-dependent,
- Tube emissivity with the applied coating was set as a function of wall temperature defined as $(-2 \times 10^{-7}T^2 + 4 \times 10^{-4}T + 0.69)$ [30],
- The convection heat transfer coefficient for the loss through the absorber to the ambient (HTC_w) was set as 10 W/m^{2}K,
- The radiation heat losses were set as the filed function upon the outer surfaces of the receivers,

According to the air velocity range, the studied flow regime was turbulent in the entire computational domain. As was already demonstrated in the literature [24], the $k-\omega SST$ (Menter) turbulence model turbulence closure with an all-y + wall treatment was selected for modeling the fluid flow in the packed RR particles. The rationale behind the choice is due to the improved performance of the $k-\omega$ model in modeling the boundary layers under adverse pressure gradients, which is pronounced in the presence of RRs [25]. Also, its higher ability than

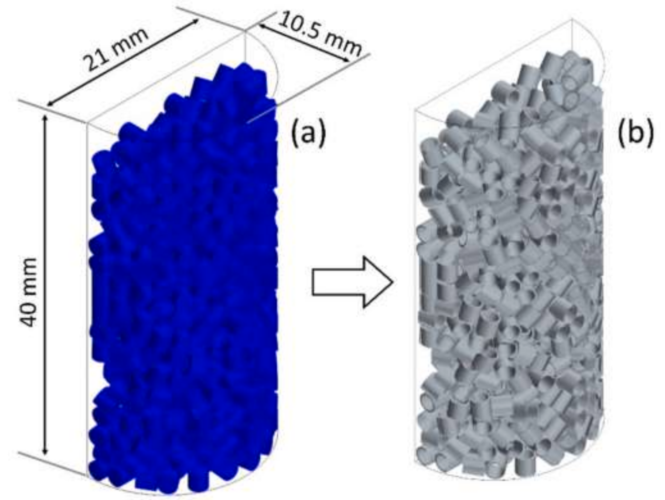

Fig. 2. Schematic of the DEM procedure for the RR matrix generation in LF50 sample; (a) DEM particles compact matrix, (b) definitive matrix after the replacement of the particles with RR.

the $k-\varepsilon$ model for predicting turbulence near walls and separated flows supports this selection. The two additional transport equations used in the $k-\omega SST$ model are presented in Eqs. (2) and (3) [31].

$$\frac{\partial}{\partial t}(\rho k)+\frac{\partial}{\partial \mathrm{x_i}}(\rho k U_\mathrm{i})=\frac{\partial}{\partial \mathrm{x_j}}\left[\left(\mu+\frac{\mu_t}{\sigma_\mathrm{k}}\right)\frac{\partial \mathrm{k}}{\partial \mathrm{x_j}}\right]+\widetilde{G_\mathrm{k}}-Y_\mathrm{k}+S_\mathrm{k} \tag{2}$$

$$\frac{\partial}{\partial t}(\rho\omega)+\frac{\partial}{\partial \mathrm{x_i}}(\rho\omega U_\mathrm{i})=\frac{\partial}{\partial \mathrm{x_j}}\left[\left(\mu+\frac{\mu_t}{\sigma_\omega}\right)\frac{\partial \omega}{\partial \mathrm{x_j}}\right]+G_\omega-Y_\omega+D_\omega+S_\omega \tag{3}$$

where $\widetilde{G_k}$ is a term for production of turbulent kinetic energy the arises due to mean velocity gradients, and is obtained as Eq. (4).

$$\widetilde{G_\mathrm{k}}=\min(G_\mathrm{k},10\rho\beta^{*}k\omega) \tag{4}$$

However, G_ω is a term for the production of ω and is defined as Eq. (5).

$$G_\omega=\frac{\alpha}{v_t}G_\mathrm{k} \tag{5}$$

The turbulence viscosity μ_t is given as Eq. (6).

$$\mu_t=\rho k\left(\min(\frac{\alpha^{*}}{\omega},\frac{a_1}{SF_2})\right) \tag{6}$$

where S represents the strain rate magnitude and α^{*} and $a_1=0.31$ are the models coefficients.

$$\alpha^{*}=F_1\alpha_1^{*}+(1-F_1)\alpha_2^{*} \tag{7}$$

In which $\alpha_1^{*}=\alpha_2^{*}=1$, and F_1 is the blending function, that combines the near-wall contribution of a coefficient with its value far away from the wall and is determined as Eq. (8) [32].

$$F_1=tanh\left(\left[min\left(max\left(\frac{\sqrt{k}}{0.09\omega d},\frac{500v}{d^2\omega}\right),\frac{2k}{d^2CD_{k\omega}}\right)\right]^{-4}\right) \tag{8}$$

where d is the distance to the wall, and $CD_{k\omega}$ displays cross-diffusion coefficient which is given as Eq. (9).

$$CD_{k\omega}=\max(\frac{1}{\omega}\nabla k.\nabla\omega,10^{-20}) \tag{9}$$

Also F_2 is the other blending function used in Eq.6 and is calculated as Eq. (10).

$$F_2=tanh\left(\left(max\left(\frac{2\sqrt{k}}{\beta^{*}\omega d},\frac{500v}{d^2\omega}\right)\right)^2\right) \tag{10}$$

while β^{*} is a model coefficient and is given as Eq. (11).

$$\beta^{*}=F_1\beta_1^{*}+(1-F_1)\beta_2^{*} \tag{11}$$

where in the simulations it was assumed that $\beta_1^{*}=\beta_2^{*}=0.09$. For the meaning of the different terms in Eqs. (2)- (11), please refer to the Nomenclature.

2.3. Grid and solution verification study

In this research, a hybrid mesh approach consisting of both structured and unstructured mesh was used to develop a reliable network grid on the solution domain. The polyhedral-based meshing with a prismatic layer for fluid regions was also employed to solve the equations. As shown in Fig. 4, custom controls were adopted to the boundary layer areas to refine the meshing with specific care, especially for the RR porous zone. While in the core area of the fluid, where the velocity and temperature gradients are smoother, cells become coarser and uniform along the length of the tube. To check the accuracy of the meshing grid, ensuring that results are independent of the number of cells, a grid independence study was carried out for the two cases of SP and PF with a PFI of 100 %. Concerning the SP, all the tube regions have been considered for the grid analysis on the outlet temperature, while only the RR region has been taken into account for the RR sample. The refinement of the grid has been achieved by first giving a constant base cell size and increasing the base cell size until $y+$ reached 1. Then, the number of prism layers was frozen, and the base cell size was decreased until convergence was achieved in the results. As a result, four different

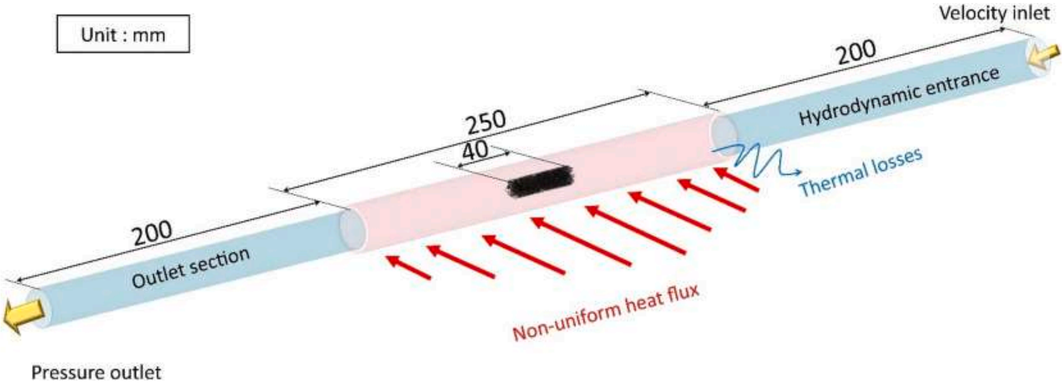

Fig. 3. Physical model and boundary conditions applied to tubular samples.

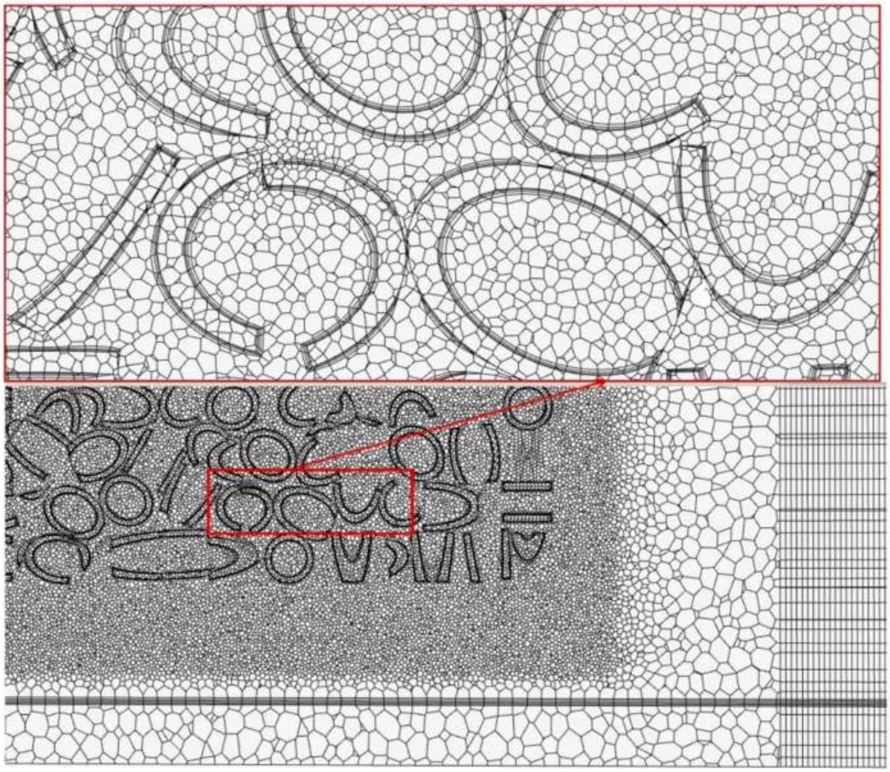

Fig. 4. Mesh network developed for the absorber with PF RR porous model.

meshes were formed for each sample ranging from the very coarse mesh to the finest mesh, comparing the pressure drops. The average cell size in Table 3 was computed as the $\sqrt[3]{V/N_{\mathrm{cell}}}$ where V is the total volume of the sample, and N_{cell} is the cell number. The grid adopted for the simulations is #3, which provides us with numerical results with less than 1 % error compared to the finest one in terms of ΔP.

2.4. Model validation

In order to assess the applicability of the developed mesh for the studied Reynolds number, the case of the smooth tube is simulated, using a constant heat load of 5000 W/m^2 and various Re and is further compared with the standard correlations in terms of Nu and f. The relevant dimensionless variables, including Re, and Nu are defined in Eq. (12) [33].

$$Re_{SP} = \frac{4m}{\pi D_i \mu}, \; Nu_{SP} = \frac{q}{\pi L k (T_w - \overline{T_a})} \tag{12}$$

where T_w is the average wall temperature obtained from the interface between the fluid and solid regions in both models. The friction factor (f) was also computed as isothermal flow as in Eq. (13).

$$\mathrm{f} = \frac{2}{L/D_{\mathrm{i}}} \frac{\Delta P}{\rho \overline{v}^2} \tag{13}$$

Table 3
Details of the results of the numerical uncertainty assessment performed for the SP and FP samples.

Sample	Mesh No.	Average cell size (mm)		$\Delta P/\Delta P_{ref}$	$\Delta T_{mo}/\Delta T_{mo,ref}$
		Fluid	*Fluid & solid*		
SP	1	0.728	0.763	0.993	0.988
	2	0.593	0.629	0.997	0.993
	3	0.506	0.540	0.998	0.992
	Base	0.418	0.452	1	1
		Fluid	*RR region*		
FP	1	0.272	0.130	0.968	1.002
	2	0.266	0.127	0.972	1.003
	3	0.253	0.122	0.980	1.004
	Base	0.220	0.104	1	1

As shown in Fig. 5a, the variations of Nu computed with the models of the current study have been plotted against Dittus-Boelter correlation [34] results for $5 \times 10^4 < Re < 10^5$. It indicates an average error of 5 %, which is within the acceptable range defined for this correlation. Fig. 5b provides the comparison of f between the CFD computed values and those that are obtained through the Petukhov correlation [35], where the average error does not exceed 4.4 %. Thus, the overall agreement is satisfactory and reflects the applicability of the numerical simulations adopted to models with the porous inserts and under the studied Re range for performance assessment purposes. It should be noted that although the inlet section is designed to ensure fully developed hydrodynamic conditions, the thermal fully developed conditions are not completely achieved within the length of the heated pipe. Therefore, the uneven differences between the numerical and empirical results can be attributed to this fact.

To validate the developed solar thermal model against the real-world data, the computed results were compared versus the measurements performed at the experimental campaign [27], in the case of a 40 mm RR porous insert completely filling the receiver (FP model), in order to assess the accuracy of the numerical models. Thus, the analyses were made based on the test results for different temperatures measured through the thermocouples welded on the tube wall at a solar peak flux of 200 kW/m^2 and Re $\sim 5 \times 10^3$. The computed CFD simulation results were also extracted from the same location of the thermocouples (TC) (Fig. 6a-b), and the inputs were per the experimental test. Fig. 6c indicates the comparison between the experimental and numerical results for the temperature increase with respect to the inlet temperature, measured at the 7 different locations of the TCs. According to the comparison between the results, CFD models have good accuracy in reproducing the experimental conditions and results within the error

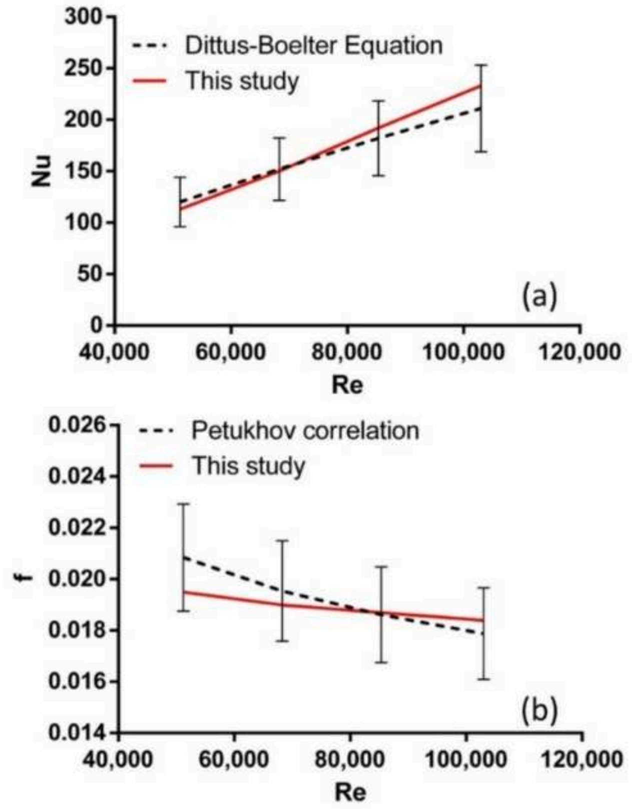

Fig. 5. Comparison of *Nu* and *f* for clear tube between the developed CFD models and standard correlations.

bars. It is worth mentioning that the numerical uncertainties were evaluated based on ASME V&V 20–2009 Standard [36], using the least squares approach. The detailed calculation process and verification methods of the implemented CFD models are already discussed in Ref. [28].

3. Heat transfer analysis

This section outlines the theoretical foundations and numerical assumptions applied in constructing the thermal model for the CFD simulations. The analyses are conducted using two distinct approaches, encompassing both the principles of the first and second laws of thermodynamics.

3.1. Energy analysis

According to [37], the spatial distribution of the solar flux in a solar furnace, is a Gaussian-shape rotationally symmetric with the peak in the center, however, in the real tests, there are some factors such as the concentrator shape and shutter blades that can influence its distribution. For simulation purposes, the concentrated solar flux imposed on the focus $E_{(S-con)}$ was considered using Eq. (14). as a function of the power on the tube perimeter [38].

$$E_{(S-con)} = \iint \varphi_{peak} \times e^{-0.5\left[\left(\frac{x}{\sigma_x}\right)^2 + \left(\frac{y}{\sigma_y}\right)^2\right]} dxdycos\theta \tag{14}$$

where φ_{peak} is the peak heat flux (W/m^2) and the amount of heat absorbed by to the solar receiver is a function of tube absorptivity coefficient (α), which can be presented as Eq. (15).

$$E_{(S-abs)} = \alpha E_{(S-con)} \tag{15}$$

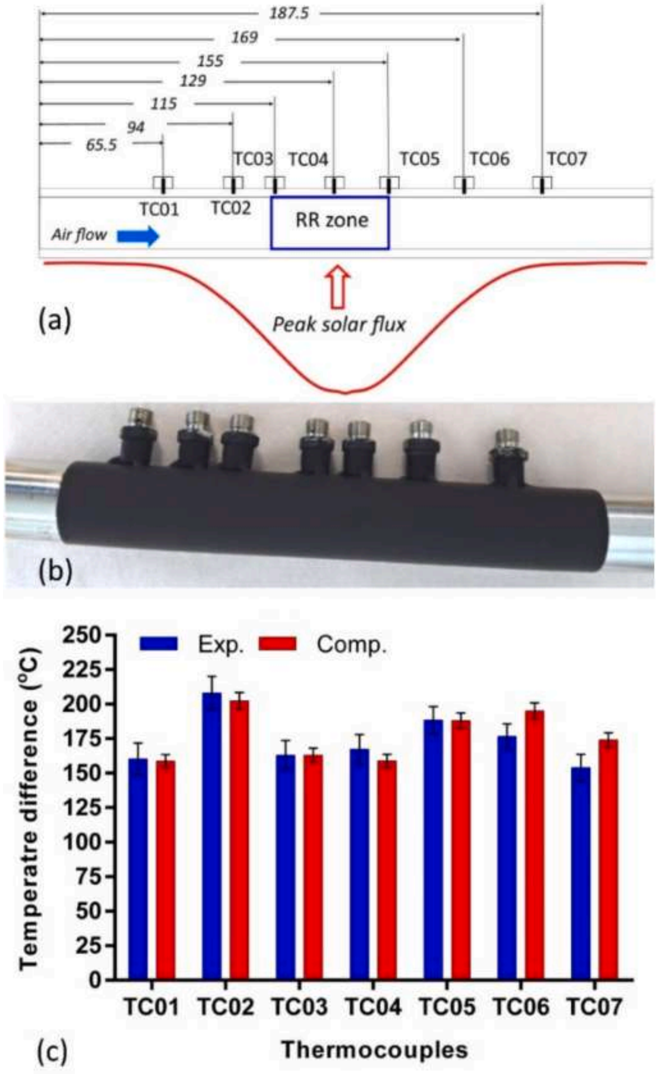

Fig. 6. (a) Locations of the thermocouples used in the experiments (values are in mm), (b) photograph of the sample used in the experiments (c) validation of the numerical study against the experimental test campaign data [27] in terms of tube wall temperature rise.

As a result, the energetic optical losses can be expressed as Eq. (16).

$$E_{l,opt} = E_{(S-con)} - E_{(S-abs)} = E_{(S-con)}(1 - \alpha) \tag{16}$$

The amount of the absorbed solar energy that is converted to the useful heat E_u can be defined as Eq. (17).

$$E_u = E_{(S-abs)} - E_{l,th} \tag{17}$$

where $E_{l,th}$ is total thermal power that is lost from the absorber to the ambient and is basically in the forms of convection $E_{l,\ conv}$ Eq. (18) and radiation losses $E_{l,\ rad}$ Eq. (19), while the conduction losses to the experimental structure are neglected.

$$E_{l,\ conv} = A_p HTC_w (T_p - T_{amb}) \tag{18}$$

$$E_{l,\ rad} = A_p \sigma \varepsilon_p (T_p^4 - T_{sky}^4) \tag{19}$$

As a result, the energetic efficiency of the absorber can be defined as the ratio between the useful power (E_u) and the total concentrated power reaching the absorber ($E_{(S-con)}$), shown in Eq. (20).

$$\eta_{en} = \frac{E_u}{E_{(S-\mathrm{con})}} \tag{20}$$

However, for more proper evaluation of a system with flow inserts in which higher useful heat production is associated with higher pumping work demand, the overall efficiency was selected according to Eq. (21).

$$\eta_{ovr} = \frac{E_u - \frac{W_P}{\eta_{el}}}{E_{(S-\mathrm{con})}} \tag{21}$$

in which W_P is the pumping work demand and can be calculated as Eq. (22).

$$W_P = \frac{m\Delta p}{\rho} \tag{22}$$

while $\eta_{el} = 32.7\ \%$ reflects the product of typical efficiencies of the power block, the electrical generator, and the fluid pump. The required pumping power is used into the calculation of thermal efficiency to account for the increased pressure losses associated with changes in absorber tubes. This inclusion ensures that the comparison process does not unfairly favour enhanced absorber tubes [39].

3.2. Exergy analysis

Exergy is a tool to quantify the quality of power of the working medium based on the environment temperature [40]. Two main assumptions needed for the exergy analysis as it is performed here are the steady-state airflow throughout the absorbers and the negligibility of potential and kinetic energies [41]. Thus, the exergy balance for a solar air heater can be expressed as Eq. (23), in which “net” denotes the net exergy rates.

$$Ex_{i,net} - Ex_{o,net} = Ex_l \tag{23}$$

whereas η_{ex}, the exergy efficiency, can be written as the ratio between the net output (desired) exergy rate to that of the net input as Eq. (24).

$$\eta_{ex} = \frac{Ex_{o,net}}{Ex_{i,net}} \tag{24}$$

Since this study focuses on exploring the role of each loss item of exergy in the specified control volume, the exergy efficiency is computed based on the loss parameter as Eq. (25).

$$\eta_{ex} = 1 - \frac{Ex_l}{Ex_{i,net}} \tag{25}$$

The net rate of exergy supplied at the inlet of the solar absorber is composed of solar radiation intensity exergy rate received on the absorber ($Ex_{(S-con)}$) and according to [42,43] the exergy rate of the solar radiation concentrated by the parabolic dish ($Ex_{(S-Cfocus)}$) can be expressed as Eq. (26).

$$Ex_{i,net} = Ex_{(S-con)} = E_{(S-con)}\left[1 + \frac{1}{3}\left(\frac{T_{amb}}{T_{sky}}\right)^4 - \frac{4T_{amb}}{3T_{sun}}\right] \tag{26}$$

where T_{sun} denotes the surface temperature of the sun and is usually predicated as 5762 K.

Exergy loss included in a solar absorber is the summation of the external exergy losses from the control volume and the rate of internal exergy losses (exergy destructions) in the control volume [44], which can be expressed as Eq. (27).

$$Ex_l = Ex_{l,ext} + Ex_{l,int} = Ex_{l,ext} + Ex_{des} \tag{27}$$

The fraction that leaves the control volume and cannot be used is external exergy loss ($Ex_{l,ext}$) which in this study accounts for the optical and thermal losses shown in Eqs. (28) and (29).

$$Ex_{l,opt} = E_{(S-con)}(1-\alpha)\left[1 + \frac{1}{3}\left(\frac{T_{amb}}{T_{sky}}\right)^4 - \frac{4T_{amb}}{3T_{sun}}\right] \tag{28}$$

$$Ex_{l,th} = E_{l,th}\left[1 - \frac{T_{amb}}{T_p}\right] \tag{29}$$

However, the exergy rates lost by flow friction, temperature difference between the source and the receiver and the fluid are internal exergy losses (exergy destruction) [45], indicated as Eqs. (30)–(32). The loss due to air friction (pressure drop) in the air ducts [46] can be expressed as Eq. (30).

$$Ex_{des,fr} = \frac{T_{amb}}{\overline{T_a}}W_p \tag{30}$$

where $\overline{T_a}$ is the mean air temperature and is determined by the average bulk fluid temperature at the inlet and the outlet ($\frac{T_o+T_i}{2}$).

The exergy destructed based on the temperature difference between the sun and solar absorber surface can be modelled as Eq. (31) [46].

$$Ex_{des,T_{sun}-T_p} = E_{(S-con)}\alpha\left[1 + \frac{1}{3}\left(\frac{T_{amb}}{T_{sun}}\right)^4 - \frac{4T_{amb}}{3T_{sun}} - (1 - \frac{T_{amb}}{T_p})\right] \tag{31}$$

The exergy destruction due to the the finite temperature difference between the absorber plate and fluid is given by Eq. (32) [47].

$$Ex_{des,T_p-T_a} = E_{(S-con)}\eta_{en}T_{amb}\left(\frac{1}{\overline{T_a}} - \frac{1}{T_p}\right) \tag{32}$$

It is important to note that both exergy efficiency and overall efficiency assess useful energy output (E_u) and work input (W_P) but with different weightings. Employing these criteria is crucial for conducting a comprehensive study, as they are more significant than flow-based criteria (e.g., the Performance Evaluation Criterion – *PEC*). This is because they consider the final yield of the system, thereby accounting for thermal losses [48,49].

4. Results and discussion

4.1. Hydraulic results

In this section, hydraulic simulations without the heat load (energy equations) are analysed to provide the details of pure fluidic behaviours of air passing through different porous inserts.

4.1.1. Flow field

The flow structure in the FP configuration has been shown in Fig. 7a, wherein the time-averaged stream wise velocity contours are computed at Q_2 flow rate. As displayed, no regular patterns are found downstream of the porous insert, where the flow discharge from the porous rear surface is affected by RR local effects. No major recirculation region exists before and after the porous block, while some reverse flow streams were merely recognized inside the porous region and based on the rings' positions. Therefore, as the fluid encounters the front surface of the porous block, it loses pressure as passing through the pore structures. Reaching the last ring layers, flow is discharged based on the blockage formation at the rear surface, creating some chaotic flow streams (Fig. 7b). Later downstream, the air flow redevelops approaching the absorber outlet. Fig. 7c displays how ring layers progressively reduce the fluid pressure at Q_2, providing a significant pressure drop over the FP insert. The values of Δp as a function of airflow rate and porous configuration are analyzed and reported in depth in section 5.1.4.2.

Fig. 8a shows the streamlines of axial velocity field computed with CFD, visualizing flow features in lateral filling insert configuration for the case of 50 % *PFI* and Q_2. The complex fluid stream through a PF porous insert can be divided into the clear flow and porous regions. As

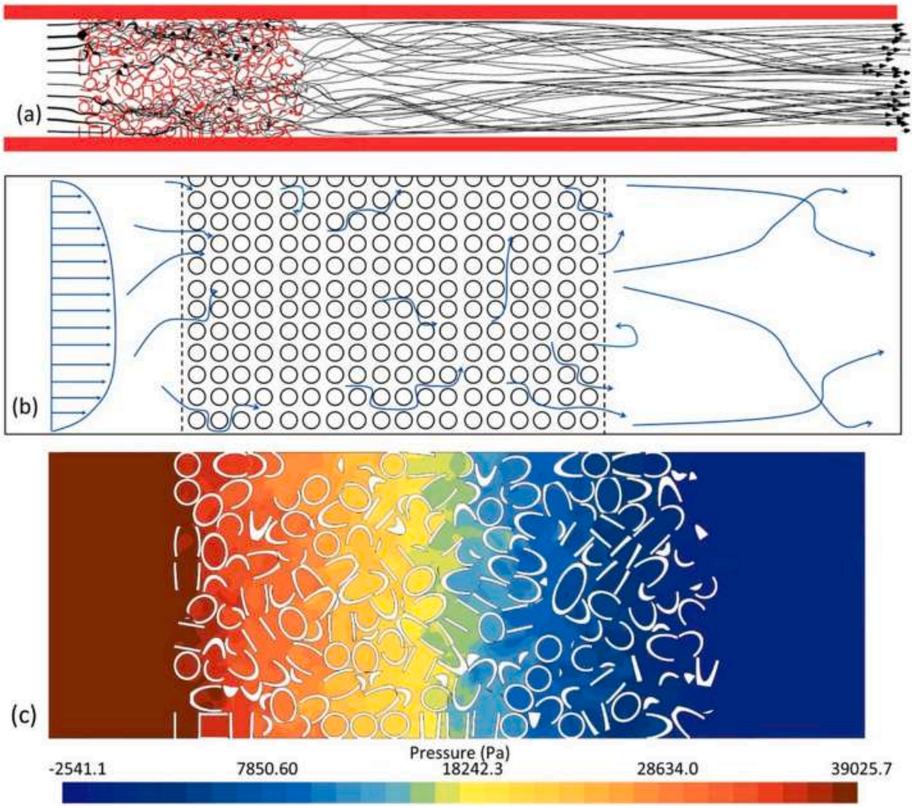

Fig. 7. Flow features for the case FP; (a) streamline contours for time-averaged flow, (b) schematic flow features, (c) pressure field obtained at Q_2.

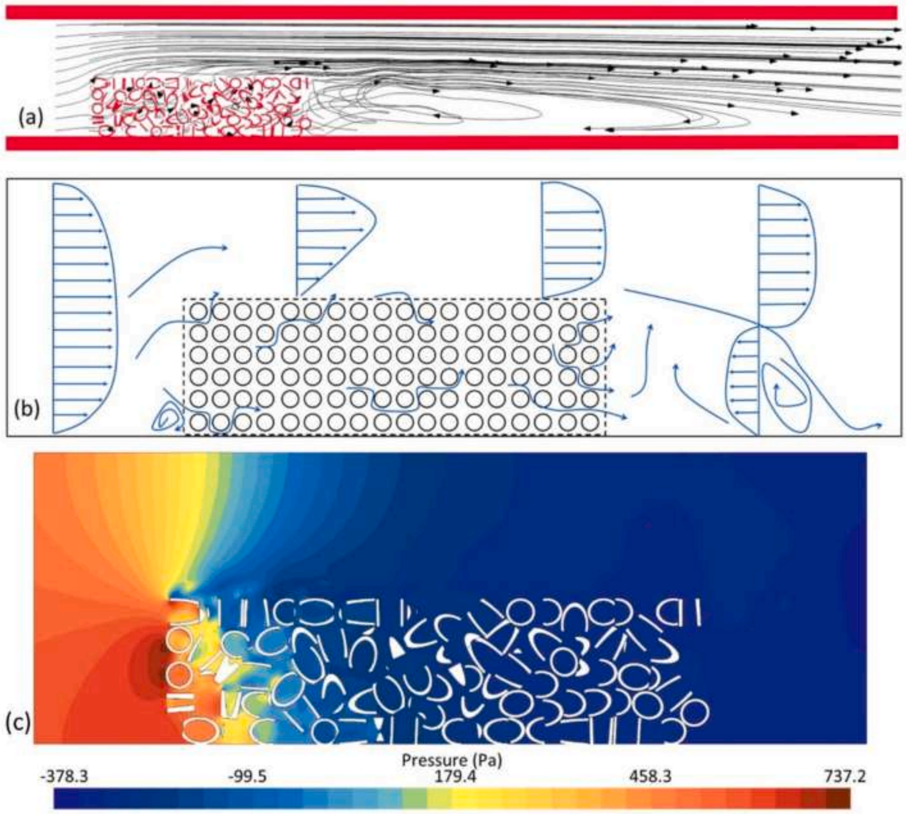

Fig. 8. Flow features for the case LF50; (a) streamline contours for time-averaged flow, (b) schematic flow features, (c) pressure filed obtained at Q_2.

the fluid reaches the porous block, it splits, and a fraction penetrates the porous zone while the other moves in the clear region and the flow redevelops after a length. A recirculation region is formed in the front edge of the porous block, while on the interface, the flow tendency is toward the clear flow region, providing a leakage from the porous body. The second recirculation region is observed downstream of the porous region, leading to a wake zone and reattachment point, the length of which depends on the fluid flow, existing from the leeward face of the porous (simplified and illustrated in Fig. 8b). These results are well-aligned with those reported by Jadidi et al. [50]. Fig. 8c presents the pressure distribution among the porous body and the clear region, highlighting a significant pressure loss on the front side of the porous block. Moreover, it also demonstrates that the fraction of the fluid that enters the porous body from the regions close to the tube wall undergoes a larger pressure loss compared to that penetrates near the clear section. This fact reflects that the fluid entering the porous region near the clear region encounters a lower resistance because of the flows through the interface, causing lower frictional losses.

Fig. 9a provides the streamlines of the axial velocity field computed with CFD, for a central filling insert configuration with 50 % *PFI* and Q_2. As observed, the flow can be divided as the fluid passing through the porous, and a bypass flow that runs around the porous insert. Shear layers were developed at the boundary between the porous insert and the bypass flow, potentially leading to mixing and turbulence depending on the flow conditions. A recirculation region is spotted in the wake, including two counter-rotating vortical flow structures. This is attributed to the fact that, after penetrating the porous body, the flow experiences a loss of pressure and establishes a recirculation region downstream of the porous insert. After coming to a reattachment point, the shear layers combine to create a developing mixing layer in the fluid core zone. The two boundary layers, from the upper and lower clear sections, interact with shedding vortex promoted by the recirculation region and form the redevelopment of mixing layer. These results follow those also found by Tan et al. [51]. It is important to mention that unlike the solid block, the wake in porous medium is detached from the trailing edge of the insert (shown in zoom section), which is due to the fluid flow across the porous body (simplified and illustrated in Fig. 9b). As a result, the two influencing parameters of porous permeability and airflow rate can govern the fluid velocity at the rear surface [52]. Therefore, when the air velocity increases, more fluid flows across the porous medium, pushing further the wake away from the rear side of the insert. Fig. 9c depicts the pressure field in the case of CF50 configuration, showing a symmetrical distribution with a pressure gradient that occurs between the fluid flowing through the porous insert and the bypass flow.

The map of velocity magnitude for the flow in the porous and clear regions has been displayed in Fig. 10, showing an uneven flow distribution along the longitudinal plane. As expected, the blockage at the porous interface compels the flow to pass through the clear region, creating high velocity values. Moreover, as the thickness of the clear region gets thinner, the velocity increases as evidenced through the comparison between LF25, LF50, and LF75, where LF75 has the highest velocity flow streams.

Fig. 11 represents the velocity field on a longitudinal section for different CF porous configurations. As seen, two quasi-symmetrical fluid streams are formed on top and bottom of the porous inserts, with high velocity due to the blockage at the core area. Thus, the fluid running the near wall area undergoes a change in boundary layer forming, which is affected by the porous fraction. CF75 with the narrowest clear region thickness promotes the highest fluid stream, forcing a considerable fraction of air passing through this area. It is also observed that, for the

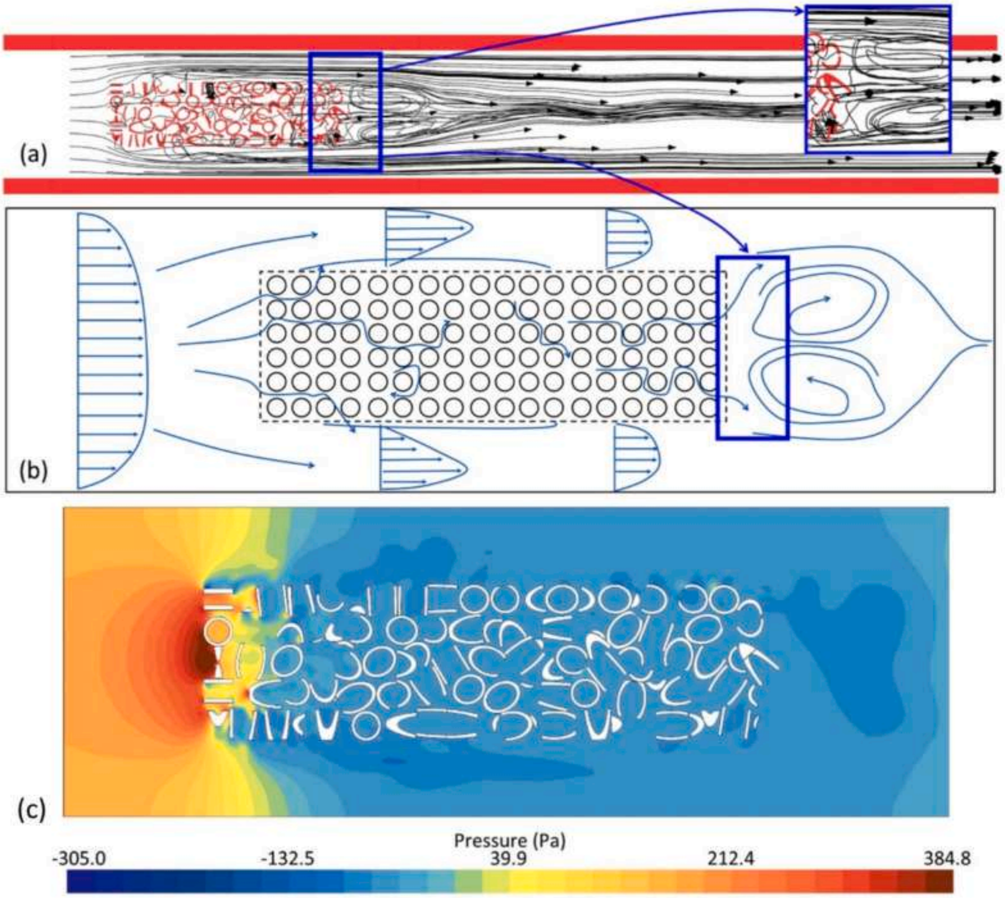

Fig. 9. Flow features for the case CF50; (a) streamline contours for time-averaged flow, (b) schematic flow features, (c) pressure filed obtained at Q_2.

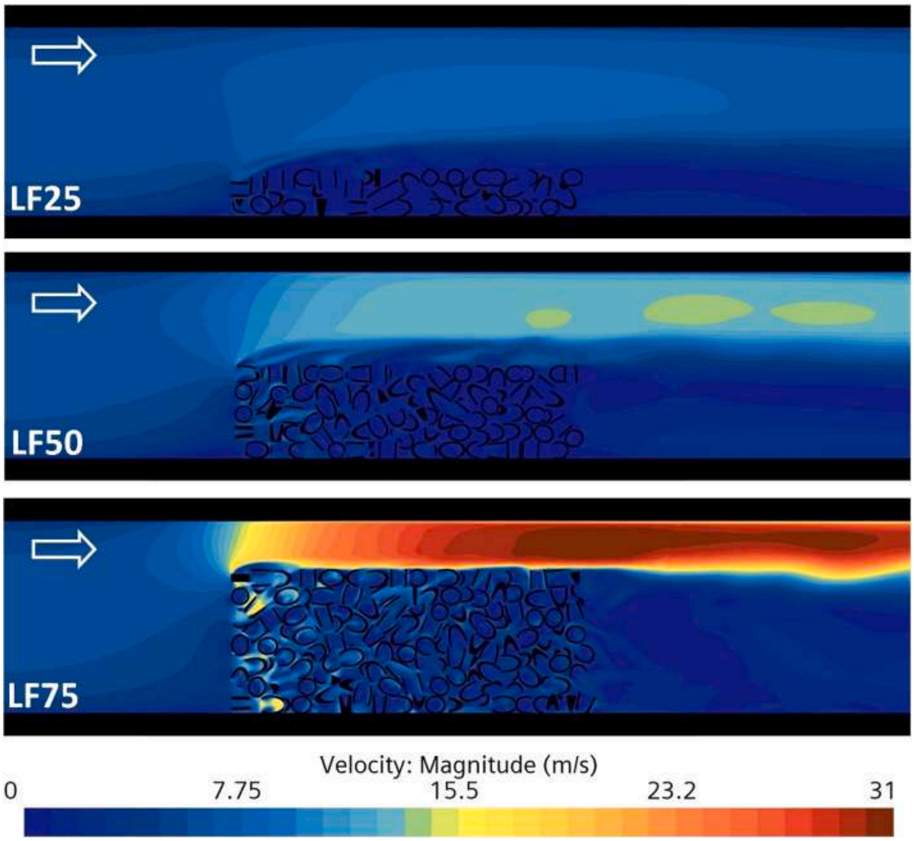

Fig. 10. Velocity field computed on a longitudinal cross section for Q_2 and various LF configurations.

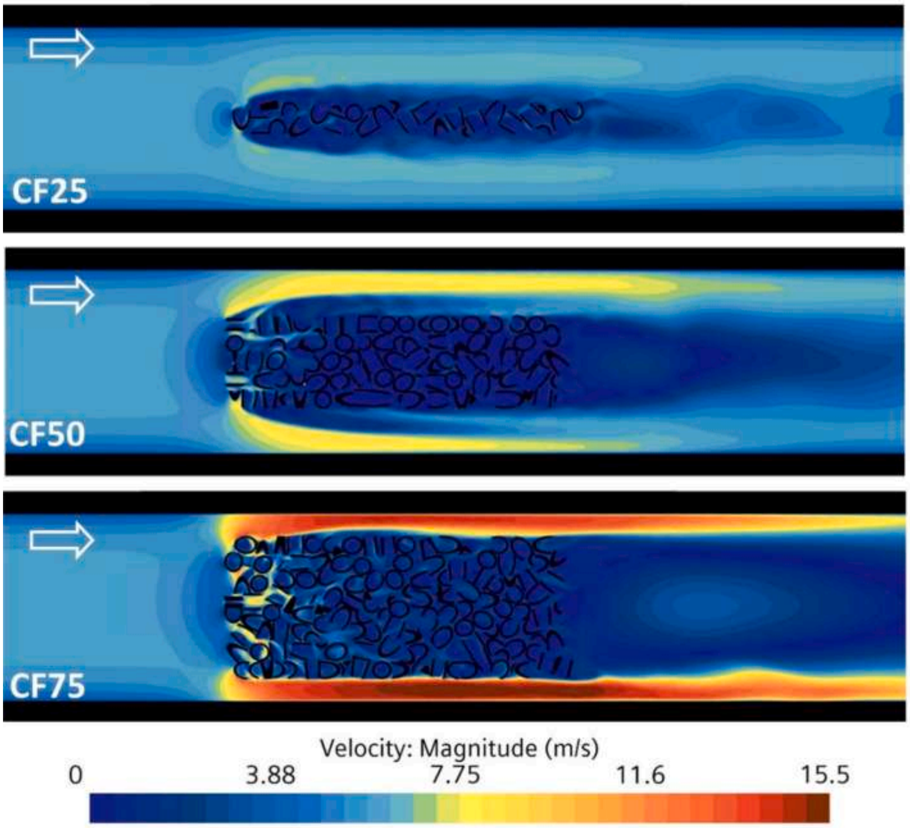

Fig. 11. Velocity field computed on a longitudinal cross section for Q_2 and various CF configurations.

three investigated cases, some high-velocity air channels are formed inside the porous medium and last from the beginning up to 25 % of the total porous length. However, the leakage and penetration from the interface affects the channels and diminishes the velocity vectors at the core of porous inserts. Analyzing the flow split among the various configurations demonstrated that nearly 71 %, 93 % and 98 % of the total fluid enter the clear region in the cases CF75, CF50, and CF25, respectively. Thus, CF porous inserts will integrate lower amounts of fluid, compared to the corresponding LF designs.

Fig. 12a presents the vertical distribution of axial velocity through and above the porous region at different porous lengths (*Z*) calculated for various LF porous integrations. The uneven shape of velocity below the interface is due to the geometric characteristics of the pores, which increases as the *PFI* grows. Analyzing the velocity magnitudes inside the porous region for $Z = 0$ shows roughly positive and > 0 values, reflecting the penetration of fluid on the porous frontal face. However, as the fluid proceeds, the axial velocity tends to decrease. Besides, the positive and negative values below the porous interface reveal the arbitrary pore structures in the RR porous matrix, which promotes flow mixing. The greater values of the LF75 case than LF50 and LF25 at the clear region refer to the higher blockage rate and smaller clear passage. As a result, an increased velocity of fluid running through RR layers is seen at LF75 than two other models for the same airflow rate. Similar analyses have been performed for the CF cases, where Fig. 12b shows the vertical distribution of axial velocity along different CF configurations. As shown, when the airflow rate increases or when the porous insert diameter grows, the axial velocity vectors in the clear region rise. Different velocity profiles extracted for various positions show that except the frontal face ($Z = 0$ mm), axial velocity is nearly 0, due to the upward or downward leakage. A deeper review of the other values of airflow rates is presented in Appendix A.

To understand the fluid behavior at the interface between porous and clear regions, several virtual planes were created during post-processing to evaluate the fluid mass flow rates at different locations. For CF designs, a co-centric cylindrical plane was formed around the porous block, and the averaged mass flow rates were computed per surface area at different longitudinal locations. For LF designs, similar data were extracted on a horizontal plane tangential to the porous top face. Fig. 13a-c shows the computed results at Q_2 versus the distance along the porous length. Positive values on the axis indicate flows outward from the planes (from the internal porous space to the clear region), while negative values indicate an inward fluid stream at the interface. In all design configurations, as the fluid penetrates the porous body, the mass flow rate values are positive, reflecting an outward flow direction (from the porous to the clear region). This is likely due to blockage effects at the porous frontal face. However, as the fluid progresses, the outward flow trend diminishes, reaching zero or an equilibrium point. Beyond this point, the average flow direction shifts inward, indicating leakage from the clear region into the porous body. Generally, when the fluid passes through the RR porous zone, stronger streams move from the porous region to the clear region, pushing the fluid stream in the clear region toward the tube wall. However, as the fluid redevelops in the clear region, the flow direction at the interface reverses and becomes negative (toward the porous region) toward the end of the porous insert. Comparing the two design concepts, CF designs reach equilibrium sooner than LF designs, due to the higher interface area in CF inserts compared to LF inserts. The location of the equilibrium point also varies with airflow rate and porous geometry. Increasing the height of the porous body pushes this point further toward the end of the porous region. This implies that thicker porous bodies promote a longer outward flow direction, resulting in stronger discharge from the porous to the clear zone compared to other designs. Furthermore, to elaborate on the flow split in the axial direction, a ratio between the flow passing through the insert (m_{PF}) and the total one was computed at Q_2 and is shown in Fig. 13d-f. As expected, with an increase in the *PFI*, the flow repartition ratio grows, with the maximum at the insert frontal surface where the

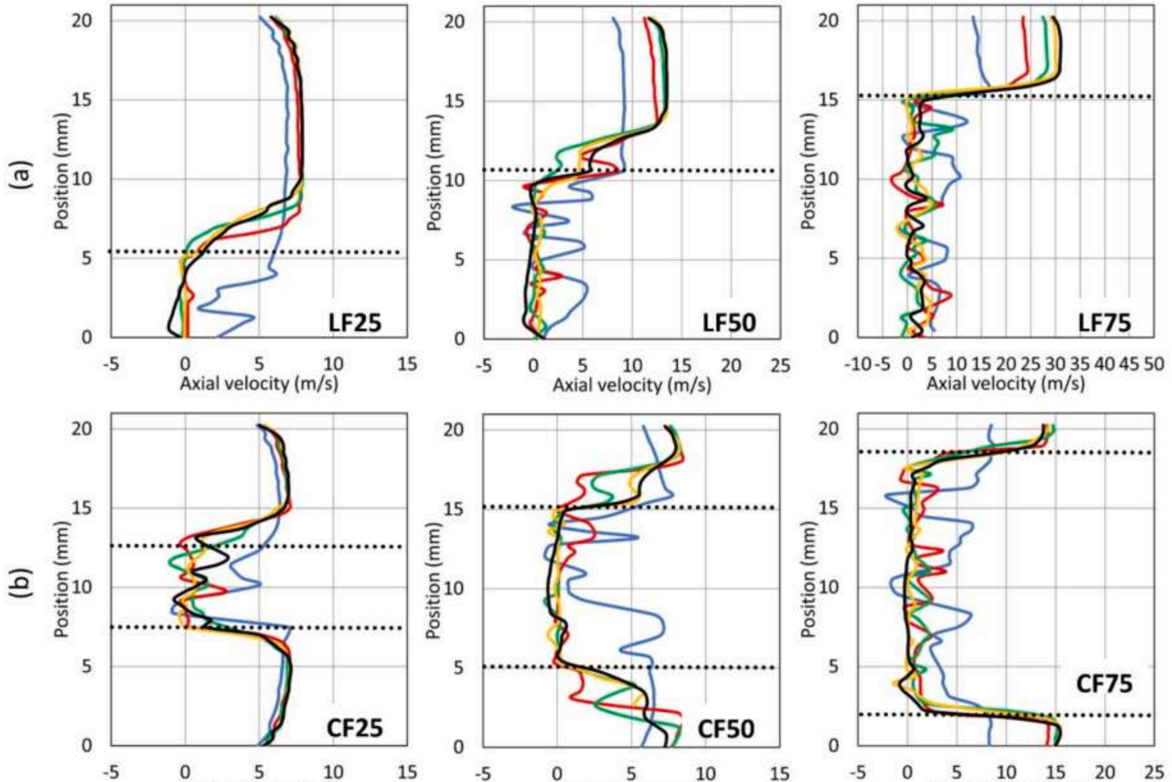

Fig. 12. Vertical distribution of axial velocity at different locations along different porous configurations at Q_2; (a) LF design, (b) CF design.

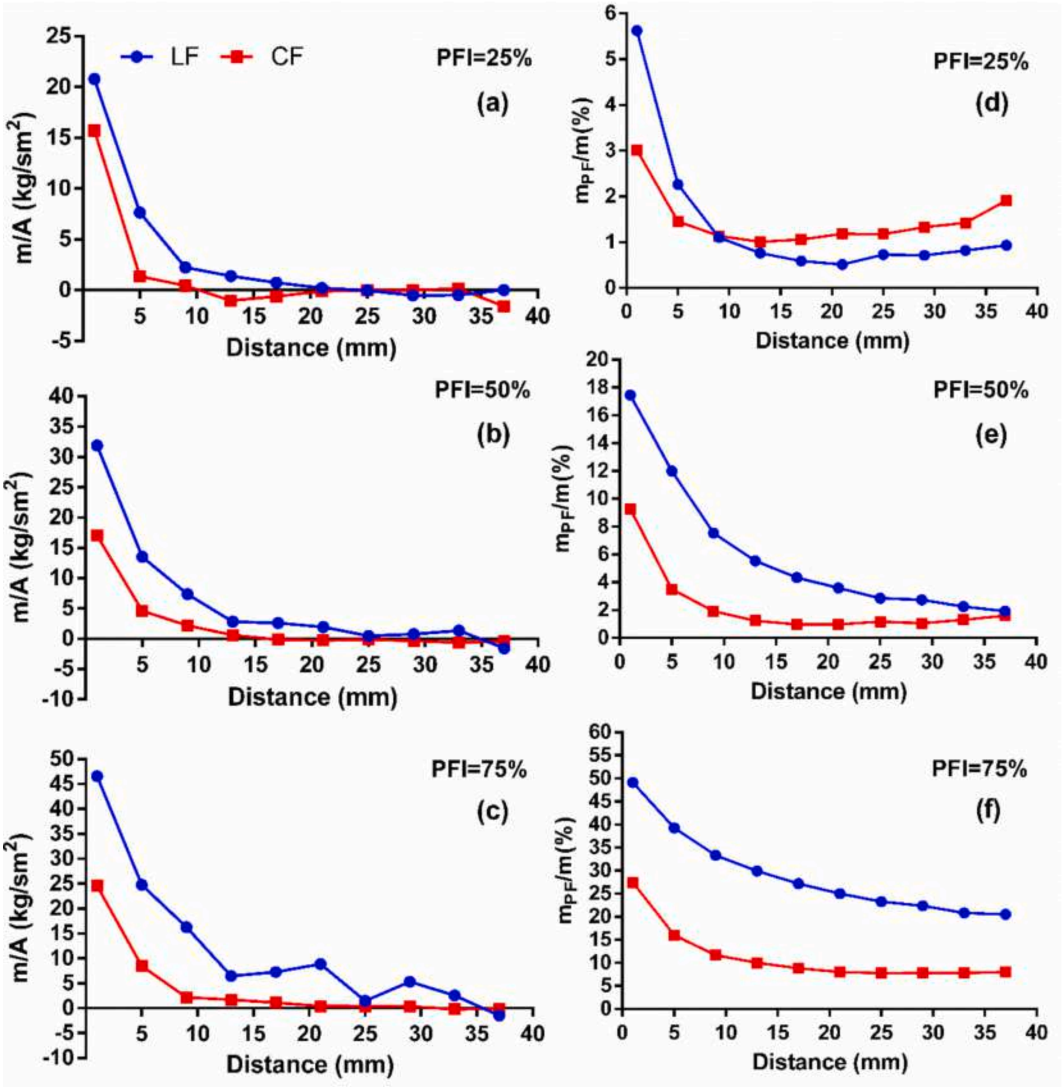

Fig. 13. Mass flow rate per surface area at the interface between the porous and clear regions at Q_2; (a) $PFI = 25$ %, (b) $PFI = 50$ %, (c) $PFI = 75$ %, flow reparation ratio computed at Q_2; (d) $PFI = 25$ %, (e) $PFI = 50$ %, (f) $PFI = 75$ %.

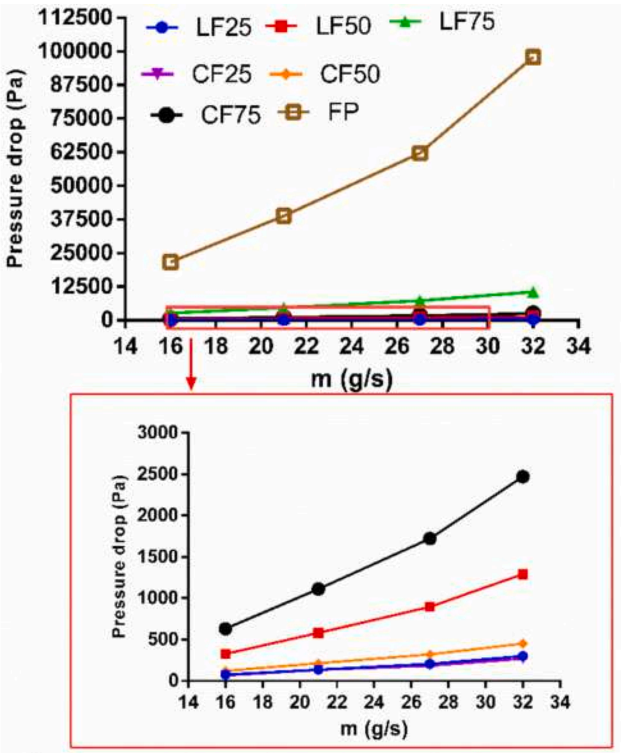

Fig. 14. Pressure drops computed for various RR integrations, depending on airflow rates.

flow has the highest kinetic energy. However, in the case of PFI = 25 % (Fig. 13d), it is observed that after an initial decrease, the flow moves from the clear zone in an inward direction, as indicated by the negative values in Fig. 13a. These conditions are met for the porous lengths > 10 mm in the case of CF, and > 20 mm in the case LF. Comparing the two designs revealed that LF inserts could hold higher amounts of fluid, resulting also in higher pressure drops. Moreover, the maximum value was achieved as 50 % in the LF75 design, which later reduces to 20 % at the end of the porous length. The data for more airflow rates are detailed in Appendix B.

4.1.2. Pressure field

Fig. 14 depicts the values of pressure drop obtained through different porous inserts. As expected the FP design with the highest volume of RR porous medium shows the maximum pressure loss at all airflow rates. Consequently, LF75 has the second highest Δp, while LF50, CF50, LF25, and CF25 are respectively presenting lower pressure losses. This confirms the efficacy of the partial-filling design in alleviating the drawbacks of RR porous insertion in increasing the pressure drop in the solar receivers. Comparing the FP design with the proposed partial filling configurations led to a minimum Δp reduction of 88 % by LF75 design and a maximum Δp reduction of 98 % by the CF25 design.

4.2. Thermal results

The data used in this section are derived from the simulations with energy equations, to obtain the overall behaviors of the proposed solar receivers.

4.2.1. Temperature fields

As shown in Fig. 15, each insert configuration provides a different cooling pattern for solid temperature distribution. In more detail, when the porous medium is attached to the tube wall, heat is conducted through the RRs and penetrates through the fluid body. Thus, the absorbed heat on the peak flux area will be dissipated more efficiently and the tube wall temperature reduced at that region. As LF and FP models provide lower temperatures at the focal point, and the solid hotspot temperature moves further from the point where the peak heat is loaded. However, the air behavior is not similar in the two mentioned models and varies based on the porous filling, where the LF design hotspot is located downstream of the porous insert, and at the FP design positions upstream. The reasons for such performances can be retraced from the flow features discussed in section 4.1.1. As already demonstrated in Fig. 8, when the air passes through a porous insert installed laterally, a fraction of fluid will pass from the clear region, making a recirculation region downstream of the insert. Thus, air will be trapped in the area formed between the porous leeward face and the recirculation region, causing a stagnation in the flow motion, which reduces the heat transfer rate from the tube wall to the fluid and provides a rise in the solid temperature. According to Fig. 7, at the FP design, when the flow exists in the porous medium, it proceeds with a chaotic behavior downstream, leading to a promoted flow with enhanced heat transfer.

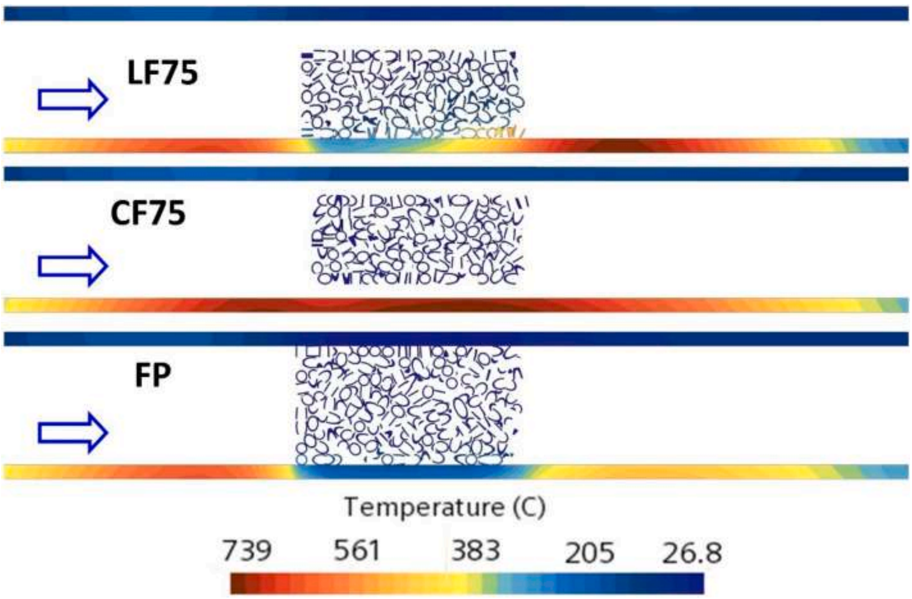

Fig. 15. Temperature field computed on a longitudinal cross section on solid domain for Q_2 and various PF configurations.

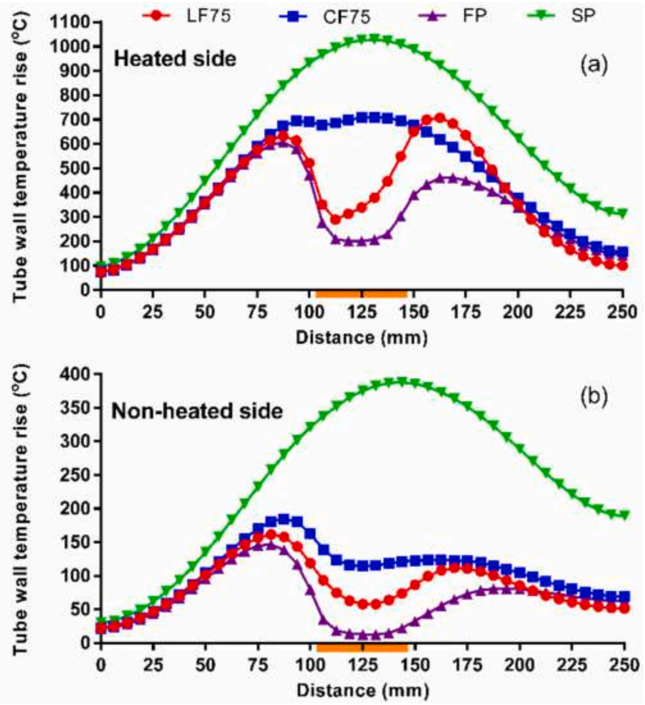

Fig. 16. Temperature rise profile computed on tube wall for Q_2 and various PF configurations; (a) heated side, (b) non-heated side. The location of the porous insert is shown in orange. (For interpretation of the references to colour in this figure legend, the reader is referred to the web version of this article.)

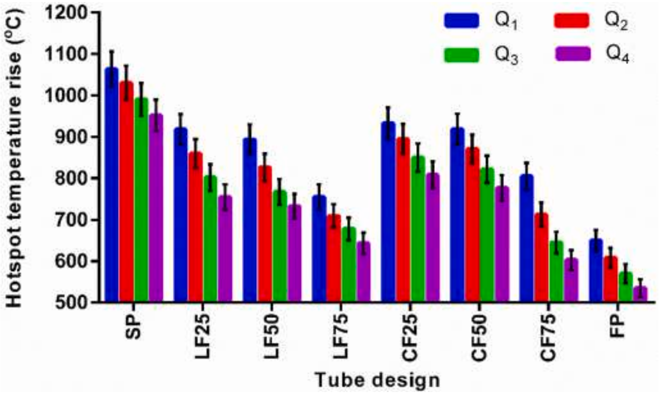

Fig. 17. Hotspot temperature rise measured on the heated side, for various PF configurations and airflow rates.

As a result, the solid temperature downstream of the insert is lower compared to the upstream, where the flow is fully developed. Finally, considering the CF design, there is no direct contact between the RR and tube wall, and the absorbed heat is transferred to the fluid through the tube's inner side. Therefore, the solid maximum temperature remains in the area where the peak heat flux is located, while the accelerated fluid streams near the tube wall will help in increasing the heat removal from the solid wall.

To elaborate on the solid temperature distribution, Fig. 16 illustrates the profiles obtained from the SP model and those with RR at Q_2. As shown in Fig. 16a, considering the heated surface, SP with no porous insert experiences the highest temperature increase compared to the other design, where the maximum is recorded as 1020 °C. However, when the RR porous insert has been integrated (FP, CF, and LF), the tube wall temperature rise is controlled and hardly reaches 700 °C. As already mentioned, FP has the lowest wall temperature, with a peak upstream of the porous region (highlighted in orange), while the LF provides the second lowest temperature rise with a peak downstream of the insert. Analysing the temperature on the other side of the pipe (see Fig. 16b), hotspots are formed upstream of the insert for all the cases with RR porous inserts, where the maximum is ~ 180 °C in the case of CF75, compared to ~ 400 °C for SP design. This implies that the thermal mixing made by the RRs in the LF75 is not similar to the heated side as there is no recirculation point on this side. Thus, air can continue transferring the heat from the tube wall to the region downstream of the insert and reduces its temperature further.

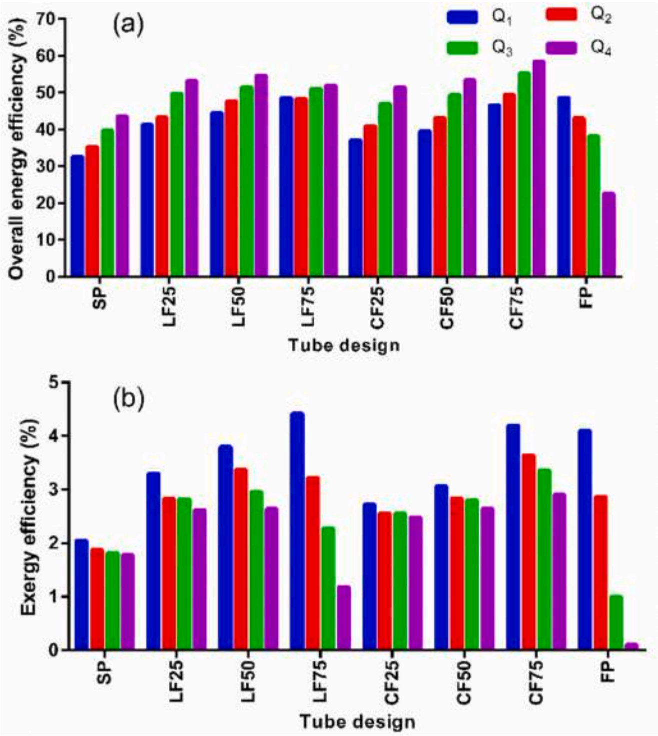

Fig. 18. Comparison of thermo-hydraulic performances obtained by various porous inserts in terms of (a) overall energy efficiency, (b) exergy efficiency.

To compare the maximum solid temperature rise achieved at different receiver designs, Fig. 17 portrays the hotspot values depending on airflow rate. As observed, an increase in the airflow rate decreases the hotspot temperature in all case studies, demonstrating greater mixing between the fluid layers, which helps in distributing heat more uniformly throughout the fluid. Moreover, SP represents the maximum hotspot values, while FP exhibits the lowest by a sharp reduction of 39 % for Q_1, and 44 % for Q_4. Comparing the two partial filling models, LF displays slightly a higher cooling effects on the hotspot compared to the CF configuration, which refers to the direct contact between the RR and the tube wall provided in this model. However, for the case of PFI = 75 %, when the air mass flow rate exceeds 16 g/s, CF75 outperforms the LF75, achieving further reduction in hotspot temperatures. The total average computed hotspot temperature decrease, with respect to the SP values, ranges from 13.5 % for CF25, to more than 30 % for both LF75 and CF75, and reaches > 40 % for the FP designs.

4.3. *Thermo-hydraulic performance*

In this section, the thermo-hydraulic performance in terms of energy and exergy approaches is presented to finalize the comparison between various porous models. The overall energy efficiency, reflecting the net energy output from the positive heat gain and the negative effects of pressure drop due to porous inserts, is depicted in Fig. 18a. These results demonstrate a reduction in energy efficiency due to the pumping energy required to compensate for friction losses caused by the porous inserts. Therefore, FP exhibits the highest reduction in energy efficiency compared to the other designs, where efficiency increases with the rise in airflow rate, averaging 32 %. The second configuration significantly affected by pressure drop is LF75, showing an average reduction in energy efficiency of 4 %. The maximum η_{ovr} is 59 %, obtained using CF75 at Q_3, while the minimum is 23 %, observed with FP integration at an air mass flow rate of 24 g/s.

Comparing the overall efficiency averaged across all airflow rates indicates that CF75, LF75, and LF50 are the top three configurations, enhancing the energetic performance of SP by 39 %, 32 %, and 31 %, respectively. Note that LF25 and LF50 outperform the corresponding CF configurations at all mass flow rates, while for the LF75 this is true only at low and moderate mass flow rates. This is easy to understand keeping in mind the discussion on the flow repartition among the different regions above. The values of the energetic thermal efficiency and the total heat losses obtained by different designs are presented and discussed in Appendix C.

According to the exergy efficiency values depicted in Fig. 18b, increasing the airflow rate negatively affects useful exergy production, resulting in a declining trend in total efficiency. Consequently, Q_1 yields the highest efficiencies for each porous configuration, with LF75 at approximately 4.5 %, FP at around 4.4 %, and CF75 at about 4.2 %, outperforming all other designs. Additionally, when the air mass flow rate exceeds 21 g/s, the exergy efficiency of the FP configuration falls below that of the SP design. Again for the exergy efficiency, the LF25 and LF50 designs outperforms the corresponding CF configurations at all mass flow rates, while for the LF75 this is true only at lowest mass flow rate, as expected from the significant increase in the pressure loss shown in Fig. 14a. A detailed exergy assessment, based on different loss and destruction sources are presented in Appendix D.

5. Conclusions

This study conducted a comparative investigation on a partially filled Raschig Ring porous insert designed for tubular solar absorbers used in concentrating solar thermal systems. Two distinct concepts, one involving lateral filling and the other central filling, were proposed and compared with full porous and simple tube designs, using computational fluid dynamic models. Fluidic and thermal characteristics were analyzed deeply to determine the most efficient configuration. Based on this analysis, the main conclusions are summarized as follows:

- Hydraulic analyses of the lateral filling design revealed that the porous insert disrupts the flow pattern and induces turbulence, leading to enhanced mixing of the fluid. However, studying the flow characteristics in the central filling design demonstrated that flow separation occurs as the boundary layer of the fluid separates from the porous surface, creating eddies and vortices downstream of the insert.
- Comparing the two partial filling techniques on thermal enhancement revealed distinct mechanisms of heat removal enhancement for lateral filling and central filling designs. In lateral filling designs, the enhancement occurs primarily due to extended heat transfer and thermal turbulence generation in the clear flow region, away from the heated side. In contrast, central filling designs benefit from thermal mixing in the core zone, coupled with turbulent flows in the annulus, which augment the heat transfer from the heated wall to the fluid.
- Evaluating the overall efficiency provides more accurate insights into the total useful energy efficiency. The results demonstrate that all proposed PF designs exhibit enhanced performance compared to the SP design. The lateral filling design with filling up to 50 % perform better than the corresponding central filling designs. Overall, the LF75 design shows an efficiency of almost 50 % at low/intermediate mass flow rate values, while the CF75 design is identified as the most efficient at high mass flow rates, with an average overall efficiency of > 50 %, reflecting an improvement of approximately 40 % over the smooth pipe design.
- The exergy efficiency, the second key performance indicator reflecting the net useful work generated through thermal enhancement and pressure drop growth, was also assessed for all designs. Results indicate that the LF25 and LF50 designs show an increase in the exergy efficiency of 50% at all considered mass flow rate values, if compared to the smooth pipe design. While the maximum value for the exergy efficiency is obtained by the LF75 configuration at the lowest mass flow rate, the CF75 design achieves the highest exergetic performance at high mass flow rates. This configuration indeed tends to reduce the exergy losses and destruction through symmetric and high-velocity fluid streams in the annulus, maintaining a controlled pressure drop.

CRediT authorship contribution statement

Hossein Ebadi: Writing – original draft, Visualization, Validation, Software, Investigation, Formal analysis, Conceptualization. **Antonio Cammi:** Writing – review & editing, Supervision, Methodology, Formal analysis. **Nima Fathi:** Writing – review & editing, Supervision, Methodology, Formal analysis. **Laura Savoldi:** Writing – review & editing, Supervision, Resources, Project administration, Methodology, Investigation, Formal analysis, Conceptualization.

Declaration of Competing Interest

The authors declare that they have no known competing financial interests or personal relationships that could have appeared to influence the work reported in this paper.

Acknowledgment

We acknowledge the use of the computational resources provided by hpc@polito, which is a project of Academic Computing within the Department of Control and Computer Engineering at the Politecnico di Torino (http://hpc.polito.it). The experimental tests have been also financed by the European Union's Horizon 2020 research and innovation program: Solar Facilities for the European Research Area – Third Phase (SFERA III) under grant agreement N. 823802.

Appendix A. . Velocity profiles

The vertical distribution of axial velocity through the porous and clear regions at different porous lengths is presented in Figs. A1 and A2, considering flow rates of Q_1, Q_3, and Q_4 for various LF and CF porous integrations.

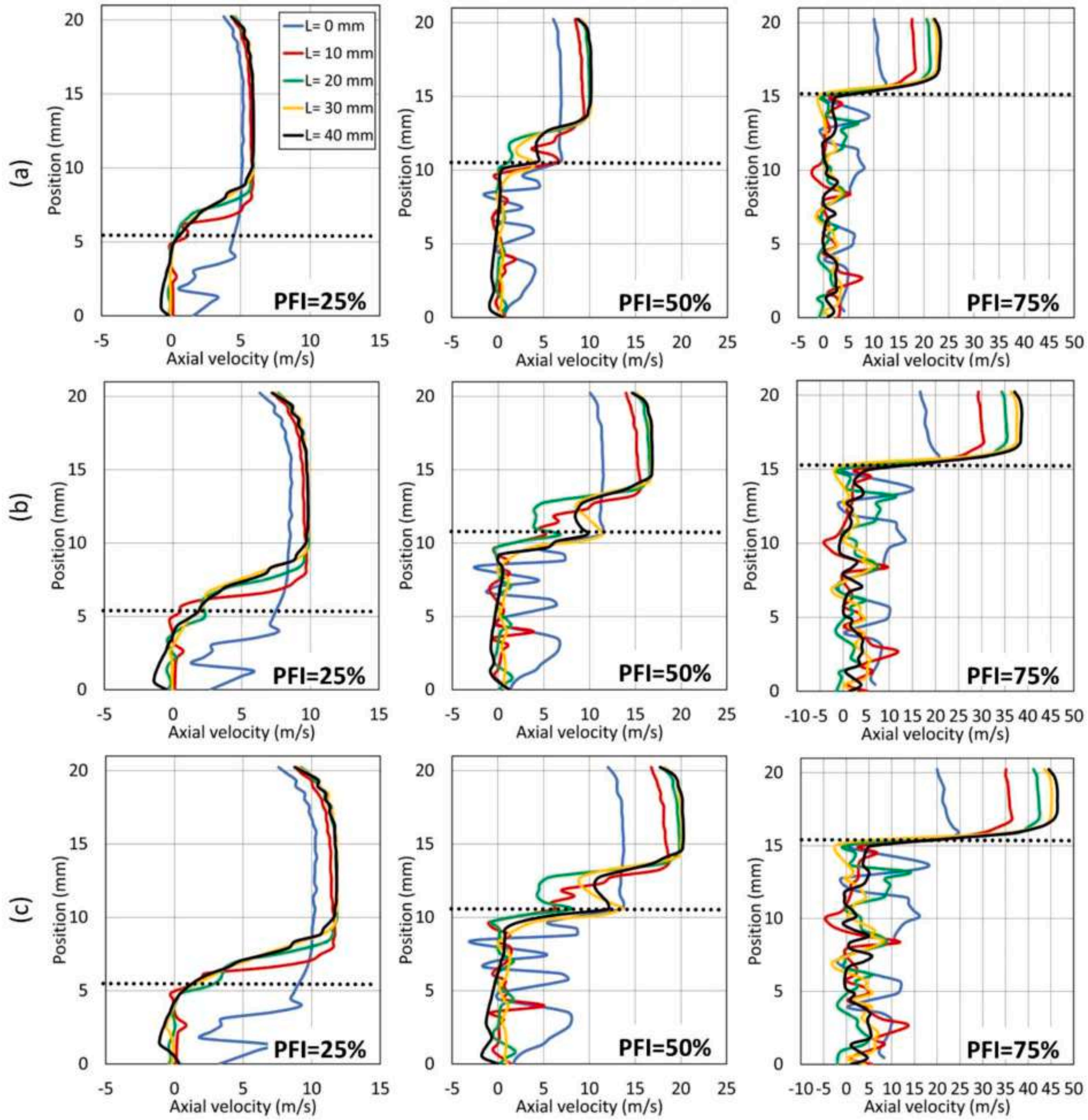

Fig. A1. Vertical distribution of axial velocity at different locations along different LF porous configurations at (a) Q_1, (b) Q_3, (c) Q_4.

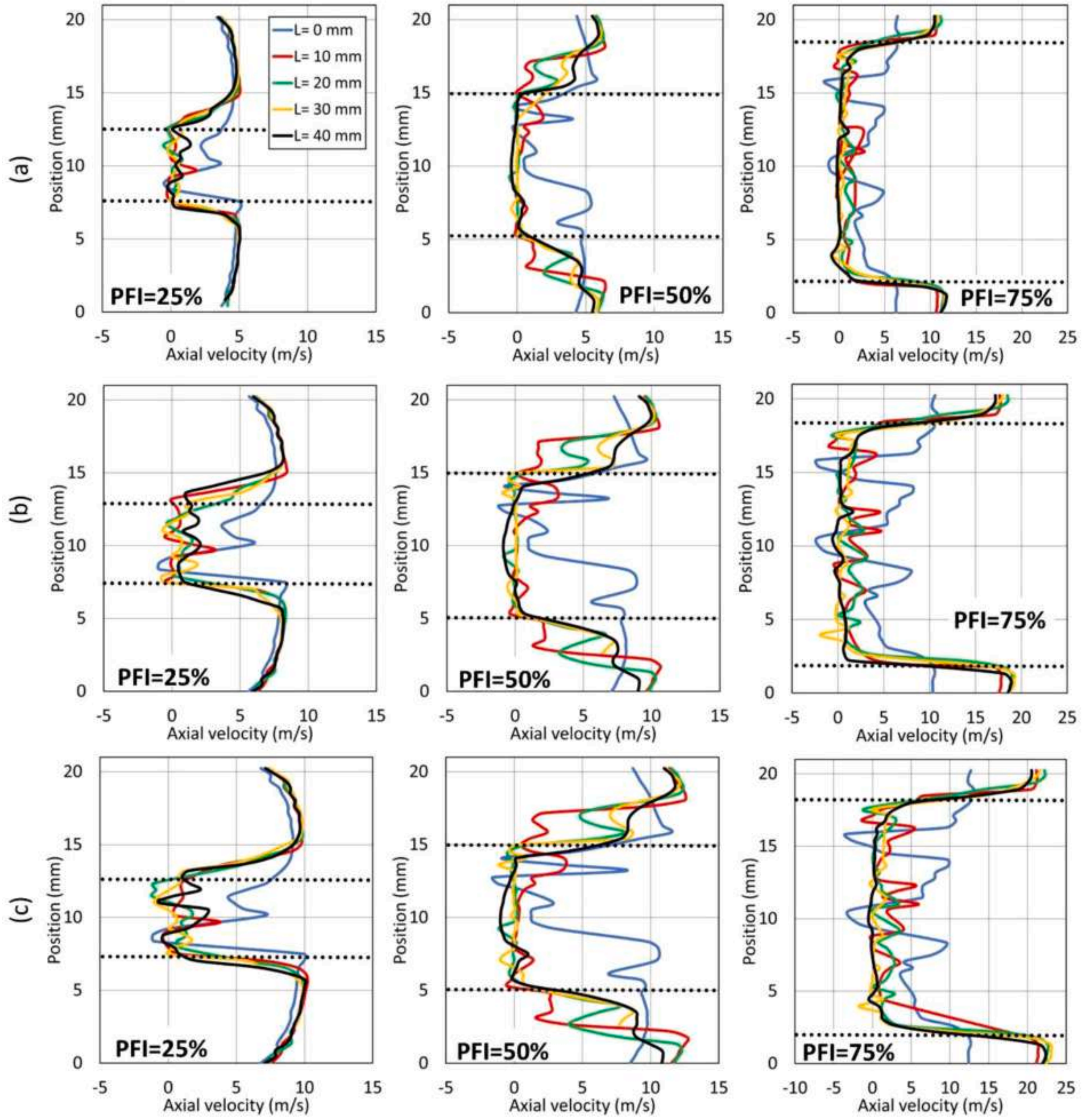

Fig. A2. Vertical distribution of axial velocity at different locations along different CF porous configurations at (a) Q_1, (b) Q_3, (c) Q_4.

Appendix B. . Flow separation between the porous and clear zones

Figs. B1–B3 provide details of the flow splits between the clear and porous zones in terms of mass flow rate per surface area and flow separation ratio, computed at flow rates of Q_1, Q_3, and Q_4 for various *PFI* values of CF and LF designs.

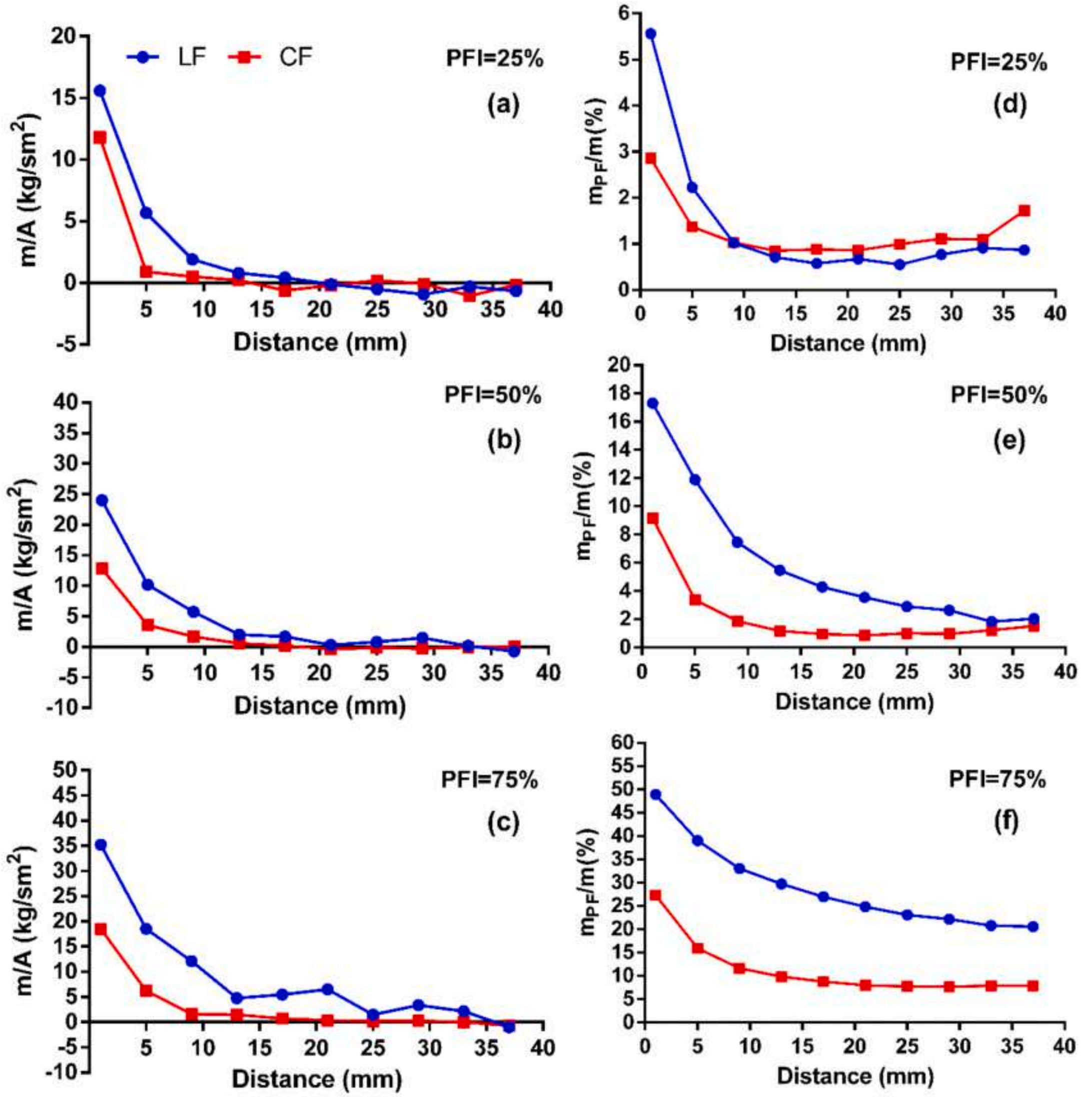

Fig. B1. Mass flow rate per surface area at the interface between the porous and clear regions at Q_1; (a) *PFI* = 25 %, (b) *PFI* = 50 %, (c) *PFI* = 75 %, flow reparation ration computed at Q_1; (d) *PFI* = 25 %, (e) *PFI* = 50 %, (f) *PFI* = 75 %.

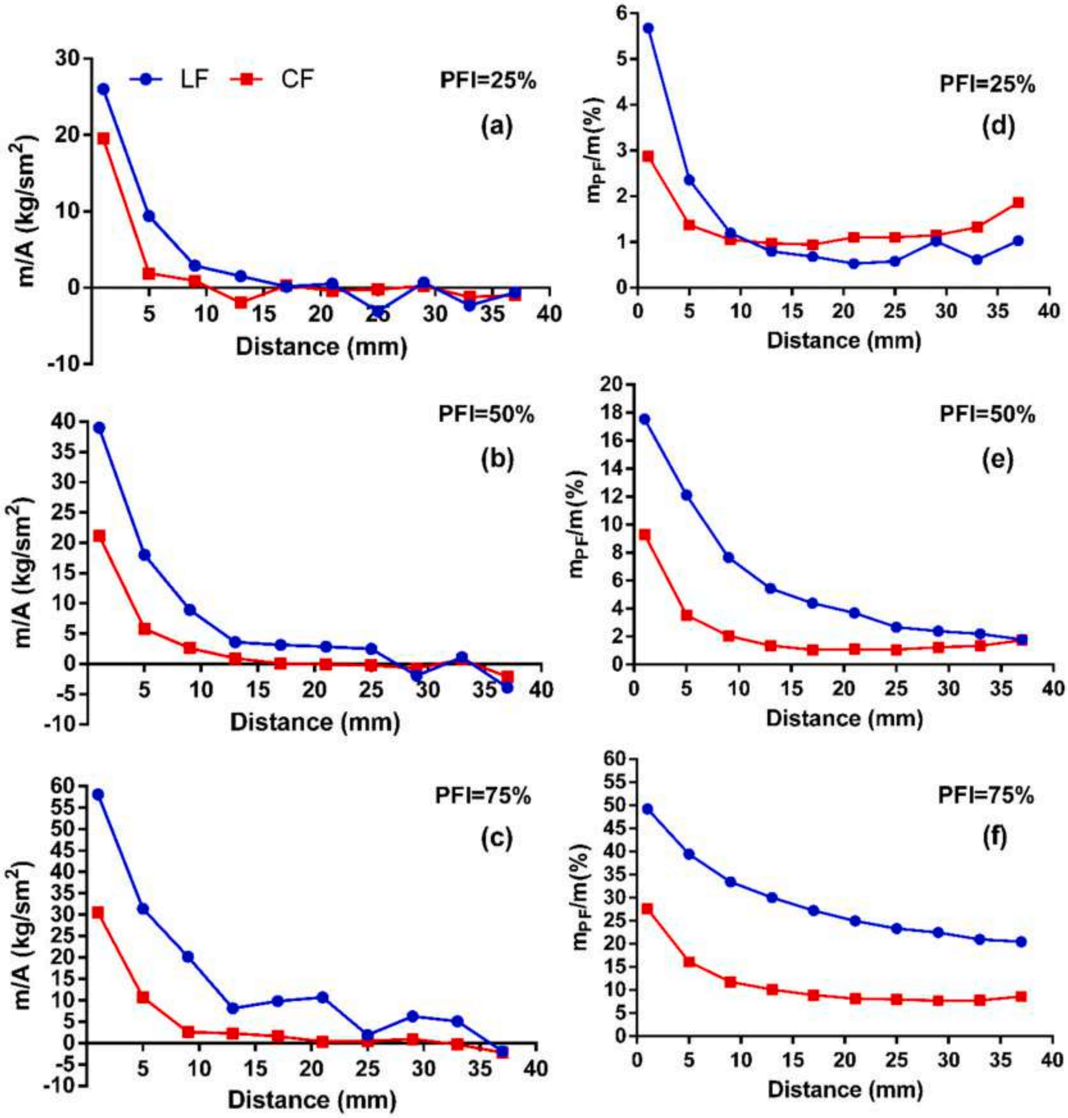

Fig. B2. Mass flow rate per surface area at the interface between the porous and clear regions at Q_3; (a) *PFI* = 25 %, (b) *PFI* = 50 %, (c) *PFI* = 75 %, flow reparation ration computed at Q_3; (d) *PFI* = 25 %, (e) *PFI* = 50 %, (f) *PFI* = 75 %.

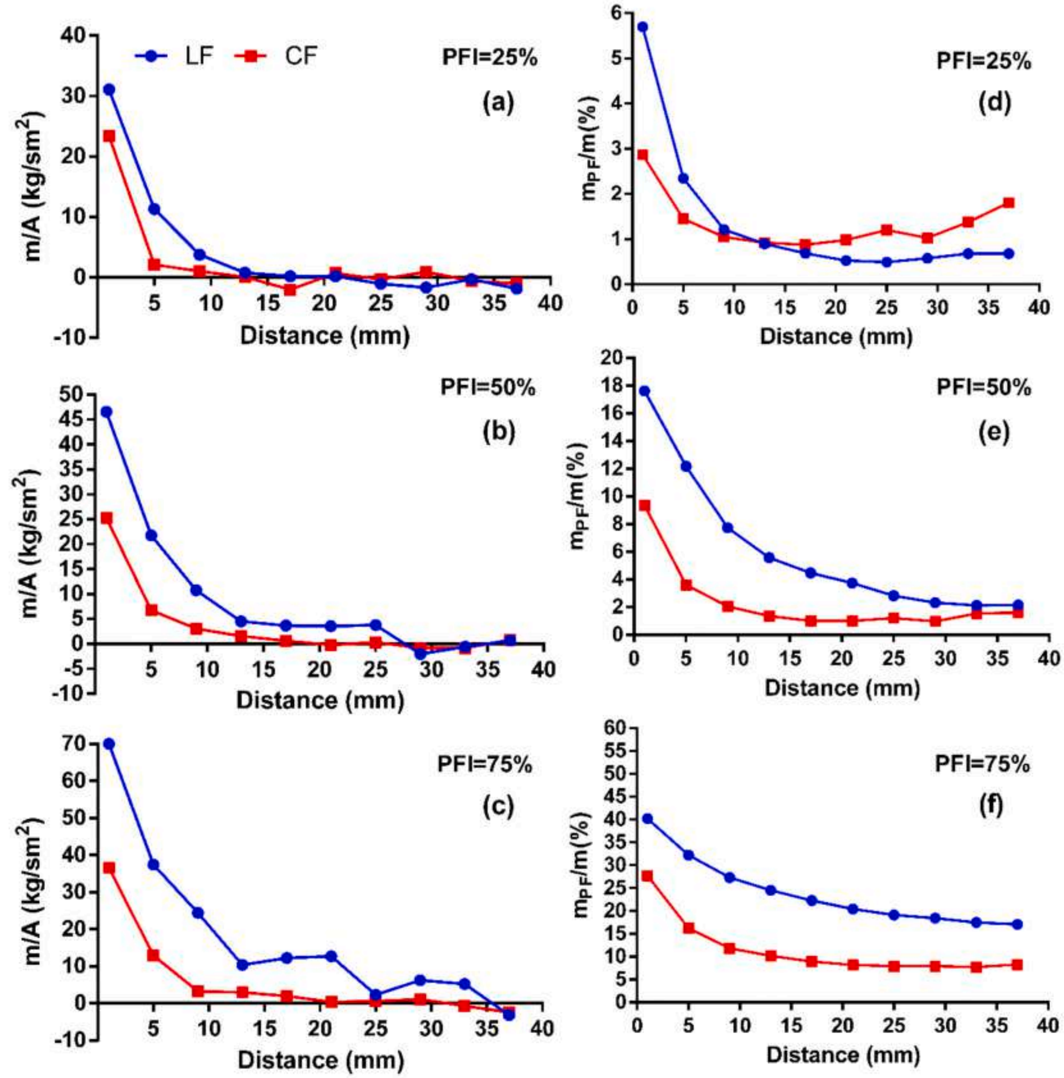

Fig. B3. Mass flow rate per surface area at the interface between the porous and clear regions at Q_4; (a) $PFI = 25$ %, (b) $PFI = 50$ %, (c) $PFI = 75$ %, flow reparation ration computed at Q_4; (d) $PFI = 25$ %, (e) $PFI = 50$ %, (f) $PFI = 75$ %.

Appendix C. . Detailed energy analysis

This section includes the energetic evaluation of the proposed solar receivers, showing more details on the total useful heat and thermal efficiencies. Fig. C1a presents the variations in the total heat loss computed for all the absorbers under different airflow rates. As observed, the increase in the airflow rate decreases the total heat lost from the absorbers, obtaining higher useful heat gain as well as increased turbulence in the heat transfer coefficient from the absorber to the running air. However, comparing the effects of various porous inserts showed that the integration of RR porous medium has decreased the thermal losses in all the proposed designs compared to the SP design. As a result, the minimum averaged thermal losses was obtained by FP as ~ 860 W and the maximum was 1240 W measured by SP. Furthermore, the maximum heat loss was obtained for SP with ~ 1350 W at Q_1 and the lowest was achieved as 742 W for FP working at Q_4. Considering the PF cases, CF75, LF75, and LF50 are the best PF designs, providing respectively 25, 23, and 20 % reduction in thermal losses compared to SP. It should also be noted that although LF75 works slightly better than CF75 at Q_1, CF75 surpasses in higher airflow rates, increasing the useful heat gain. This phenomenon can be traced back from the hydraulic analysis, discussed in Figs. 10 and 12. In more detail, when the airflow rate increases, fluid streams runs near the heated surface show different responses in CF75 and LF75. Thus, in the case of CF75, higher airflow rates provide an accelerated bypass flow in the annulus region, especially at boundary layers close to the heated wall, which significantly improves the heat exchanged at that region. While in the case of LF75, higher air flux slightly changes the fluid velocity at the voids of the porous structure located next to the heated wall, leading to a slight heat transfer improvement.

Fig. C1b shows the variations in the energy efficiency based on the studied cases and various airflow rates. As expected, SP has the lowest efficiency at all airflow rate levels due to the higher absorber wall temperatures, resulting in significant radiation and convection losses. However, FP provides the highest efficiency at each airflow level, followed by CF75 and LF75. Analyzing the improvement effects of various porous integrations over the simple design, it was found that a 50 % higher efficiency can be achieved as an average among all the studied flow rates using FP design. Furthermore, decreasing the porous integration from 100 to 75 %, the central filling enhances the efficiency by 40 % while lateral filling reflects a 38 % improvement. Considering 50 % filling ration, the enhancement effect reduces to 32 and 23 %, respectively using LF and CF concepts. Finally, the minimum efficiency augmentation is achieved at 25 % filling ration, displaying 17 and 27 % for the cases of CF and LF, respectively. As a result, CF provides an enhanced performance at higher filling ration while LF reflects superiority at lower filling ratio.

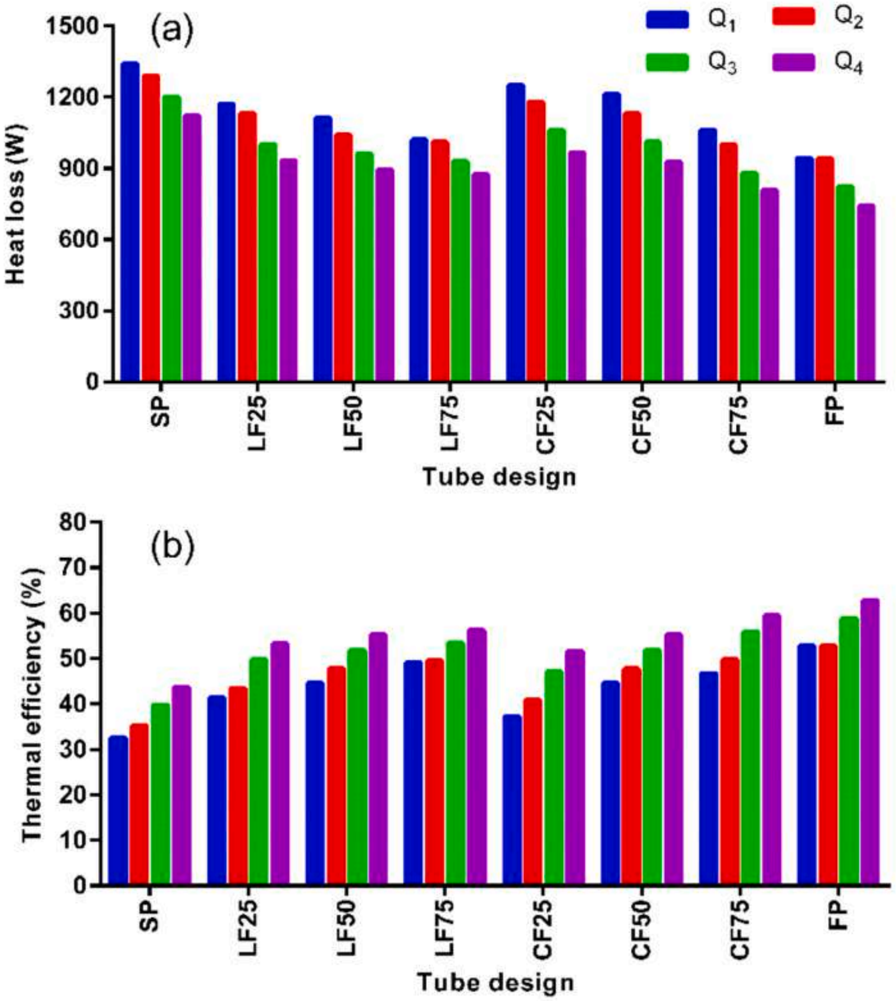

Fig. C1. Comparison of thermal performances obtained by various porous inserts in terms of (a) heat loss power, (b) thermal efficiency.

Appendix D. . Detailed exergy analysis

To perform the exergy analysis on the studied cases, it is crucial to present the variation of different exergy loss terms against the testing conditions to identify the most and least significant terms. For better comparison, these values are normalized by the net inlet exergy of the sun. Fig. D1 shows the computed terms for all the porous configurations. According to figure D1a, the optical-related loss ($Ex_{l,opt}/Ex_{i,\,net}$) is a major source of exergy loss, consistently accounting for approximately 5 %, regardless of the absorber design.

The other significant source of exergy loss is due to heat losses ($Ex_{l,th}$), which accounts for 10 % to 30 % of the total inlet exergy, depending on the absorber design. As shown in figure D1b, increasing the airflow rate positively impacts and reduces $Ex_{l,th}/Ex_{i,\,net}$. The SP configuration without a porous insert exhibits the highest exergy loss rate, reaching up to 40 %, while the FP configuration reduces this term to below 20 %. The results also indicate that LF75 has the second lowest exergy loss due to heat loss, followed by CF75 and LF50. This trend is attributed to enhanced heat transfer from the absorber tube to the fluid, resulting in lower thermal losses between the absorber and the ambient. Consequently, RR porous integration significantly reduces exergy losses arising from thermal losses.

Fig. D1c displays the fraction of inlet exergy destroyed due to the temperature difference between the absorber surface and the sun ($Ex_{des,Tsun-Tp}$). The results indicate that as heat dissipation improves with increased flow rate, the absorber temperature decreases, leading to increased exergy destruction. Additionally, the insertion of porous materials intensifies $Ex_{des,Tsun-Tp}/Ex_{i,\,net}$, resulting in a greater temperature difference between the absorber and the sun. Consequently, compared to the SP design, the smallest increase in exergy destruction was 13 % with CF25, while the largest increase was 60 % with FP integration.

Considering the exergy destruction in the heat flow from the absorber to the fluid, figure D1d shows the performance of various absorber designs. As observed, the airflow rate can exhibit three different roles depending on the absorber design, due to the trade-off between thermal efficiency and the temperature difference between the absorber and the fluid. For the SP, CF25, CF50, and LF25 designs, which have lower energy efficiency compared to other designs, increasing the airflow rate enhances exergy destruction due to the increased temperature differences between the fluid and absorber. In contrast, for the LF50, LF75, and CF75 designs, the rise in airflow rate has minimal impact on exergy destruction in the heat flow from the absorber to the fluid. However, in the FP design, which has the highest energy efficiency, increasing the airflow rate reduces exergy destruction by enhancing the heat transfer coefficient between the fluid and absorber, thereby lowering the temperature difference between the fluid and receiver.

Consequently, integrating a porous insert effectively reduces $Ex_{des,Tp-Ta}/Ex_{i,\,net}$ when using the LF50 and CF75 configurations at an air mass flow rate above 21 g/s, or when using the LF75 and FP configurations at all airflow rate levels.

According to figure D1e, the fraction of exergy destroyed by air friction inside the absorbers was computed relative to the inlet exergy. As expected, increasing the airflow rate increases exergy destruction due to pressure losses. Additionally, as the porous index increases, $Ex_{des,fr}/Ex_{i,\,net}$ rises, highlighting the impact of flow behavior through different porous inserts on exergy destruction. Consequently, the FP design exhibits the highest destruction share, ranging from 1 % to 3.5 %, while the CF25 design has the lowest, between 0.005 % and 0.042 %. Furthermore, the LF configuration contributes more significantly to total exergy destruction due to flow friction compared to the CF configuration.

In conclusion, results demonstrated that $Ex_{des,Tsun-Tp}$ is the primary source of exergy reduction, followed by $Ex_{l,th}$, $Ex_{des,Tp-Ta}$, $Ex_{l,opt}$ and $Ex_{des,fr}$, respectively. Therefore, CF75 emerged as the most efficient configuration within the studied airflow range, where $Ex_{des,Tsun-Tp}$ improved by $\sim$ 37 %, $Ex_{l,th}$ decreased by $\sim$ 43 %, $Ex_{des,Tp-Ta}$ remained nearly constant, and $Ex_{des,fr}$ increased by $>$ 800 % than SP design.

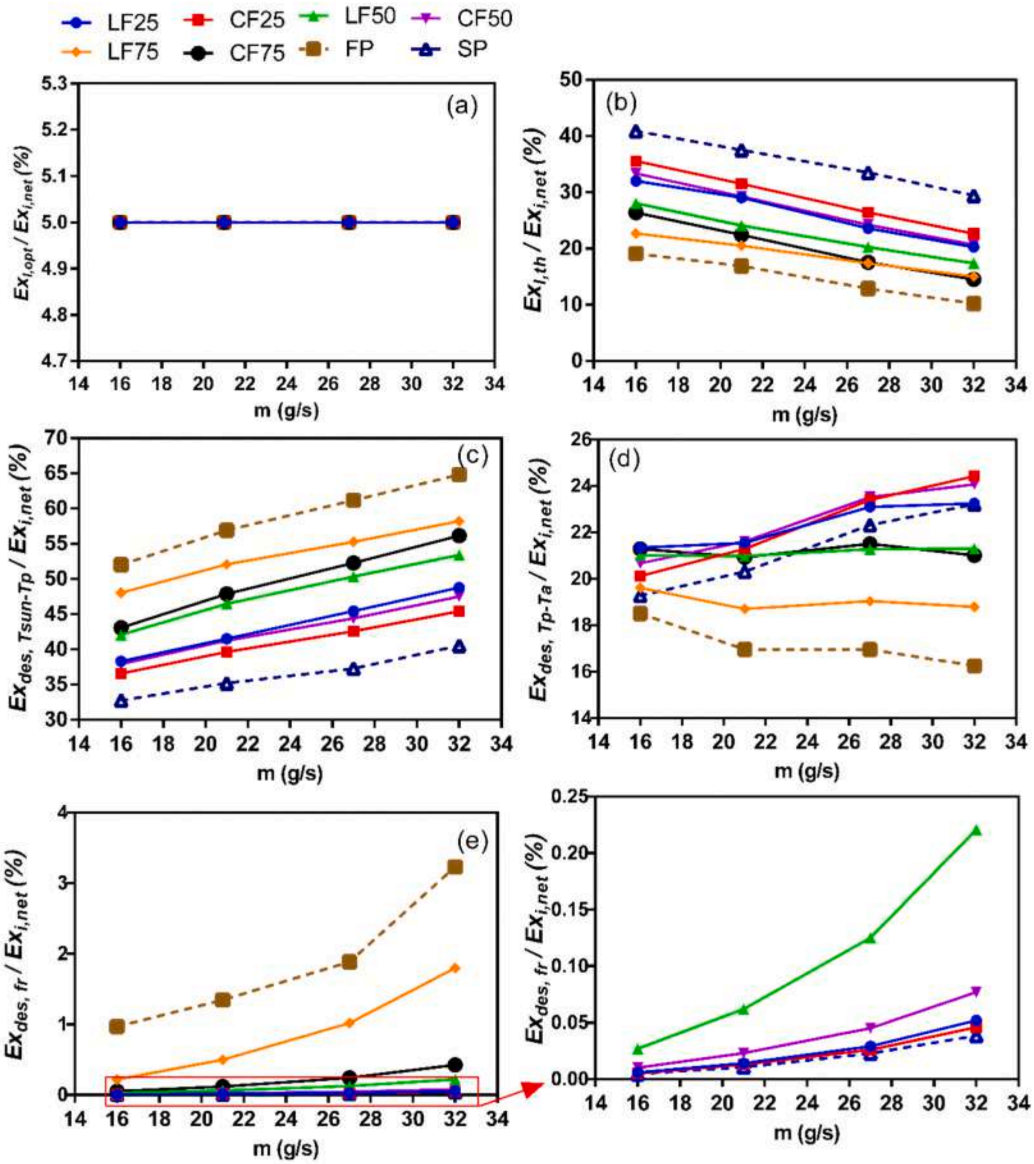

Fig. D1. Variations exergy loss terms divided by input solar exergy based on; (a) optical loss, (b) thermal loss, (c) temperature difference between the sun and solar absorber surface, (d) finite temperature difference between the absorber and fluid, (e) air friction for the various solar absorbers.

References

[1] M. Sedighi, R.V. Padilla, R.A. Taylor, M. Lake, I. Izadgoshasb, A. Rose, High-temperature, point-focus, pressurised gas-phase solar receivers: A comprehensive review, Energy Convers. Manag. 185 (2019) 678–717, https://doi.org/10.1016/j.enconman.2019.02.020.

[2] M. Cantone, M. Cagnoli, J. Fernandez Reche, L. Savoldi, One-side heating test and modeling of tubular receivers equipped with turbulence promoters for solar tower applications, Appl. Energy. 277 (2020) 115519, https://doi.org/10.1016/j.apenergy.2020.115519.

[3] Z.-J. Zheng, M.-J. Li, Y.-L. He, Thermal analysis of solar central receiver tube with porous inserts and non-uniform heat flux, Appl. Energy. 185 (2017) 1152–1161, https://doi.org/10.1016/j.apenergy.2015.11.039.

[4] M. Hazmoune, B. Aour, X. Chesneau, M. Debbache, D.-A. Ciupageanu, G. Lazaroiu, M.M. Hadjiat, A. Hamidat, Numerical Analysis of a Solar Tower Receiver Novel Design, Sustainability. 12 (2020), https://doi.org/10.3390/su12176957.

[5] S. Hatcher, R. Khadka, B. Pidaparthi, S. Missoum, P. Li, B. Xu, Multiphysics Numerical Study of Solar Receiver Tube for Enhanced Thermal Efficiency and Durability in Concentrated Solar Power Tower Plant (2022), https://doi.org/10.1115/ES2022-81009.

[6] F. Haddad, B. Pidaparthi, N.N. Afrin, S. Missoum, J. Li, B. Xu, P. Li, Flow and Heat Transfer Experimental Study for 3D-Printed Solar Receiving Tubes With Helical Fins at Internal Surface, J. Sol. Energy Eng. 147 (2024), https://doi.org/10.1115/1.4065657.

[7] H. Ebadi, A. Cammi, L. Savoldi, Energetic and Exergetic Analyses of a Double-Pass Tubular Absorber for Application in Solar Towers, J. Sol. Energy Eng. 146 (2024), https://doi.org/10.1115/1.4066201.

[8] S. Rashidi, J.A. Esfahani, A. Rashidi, A review on the applications of porous materials in solar energy systems, Renew. Sustain. Energy Rev. 73 (2017) 1198–1210, https://doi.org/10.1016/j.rser.2017.02.028.

[9] H. Peng, M. Li, X. Liang, Thermal-hydraulic and thermodynamic performance of parabolic trough solar receiver partially filled with gradient metal foam, Energy 211 (2020) 119046, https://doi.org/10.1016/j.energy.2020.119046.

[10] M.A. Al-Nimr, M.K. Alkam, A modified tubeless solar collector partially filled with porous substrate, Renew. Energy. 13 (1998) 165–173, https://doi.org/10.1016/S0960-1481(97)00047-5.

[11] N.F. Jouybari, T.S. Lundström, Performance improvement of a solar air heater by covering the absorber plate with a thin porous material, Energy 190 (2020), https://doi.org/10.1016/j.energy.2019.116437.

[12] S. Singh, Utilising fractional porous interface for high thermal performance of serpentine wavy channel solar air heater, Appl. Therm. Eng. 205 (2022) 118044, https://doi.org/10.1016/j.applthermaleng.2022.118044.

[13] M.V. Bozorg, M. Hossein Doranehgard, K. Hong, Q. Xiong, CFD study of heat transfer and fluid flow in a parabolic trough solar receiver with internal annular porous structure and synthetic oil–Al2O3 nanofluid, Renew. Energy. 145 (2020) 2598–2614, https://doi.org/10.1016/j.renene.2019.08.042.

[14] C. Yang, W. Liu, A. Nakayama, Forced Convective Heat Transfer Enhancement in a Tube with its Core Partially Filled with a Porous Medium, Open Conserv. Biol. J. 1 (2009) 1–6, https://doi.org/10.2174/1877729500901010001.

[15] N.F. Jouybari, M.E. Nimvari, W. Zhang, A comparative study of different heat transfer enhancement mechanisms in a partially porous pipe, SN Appl. Sci. 3 (2021) 798, https://doi.org/10.1007/s42452-021-04782-3.

[16] M. Akbarzadeh, S. Rashidi, A. Keshmiri, N. Shokri, The optimum position of porous insert for a double-pipe heat exchanger based on entropy generation and thermal analysis, J. Therm. Anal. Calorim. 139 (2020) 411–426, https://doi.org/10.1007/s10973-019-08362-x.

[17] H.E. Ahmed, O.T. Fadhil, M.G. Jehad, M.A. Alfellag, Enhancement of Thermal Design of Pipe Filled Partially with Porous Media Using Eccentric Fluid Cores, Arab. J. Sci. Eng. 47 (2022) 16171–16186, https://doi.org/10.1007/s13369-022-06815-4.

[18] F. Shikh Anuar, I. Ashtiani Abdi, K. Hooman, Flow visualization study of partially filled channel with aluminium foam block, Int. J. Heat Mass Transf. 127 (2018) 1197–1211, https://doi.org/10.1016/j.ijheatmasstransfer.2018.07.047.

[19] M. Nazari, M.H. Kayhani, R. Mohebbi, HEAT TRANSFER ENHANCEMENT IN A CHANNEL PARTIALLY FILLED WITH A POROUS BLOCK: LATTICE BOLTZMANN METHOD, Int. J. Mod. Phys. c. 24 (2013) 1350060, https://doi.org/10.1142/S0129183113500605.

[20] S. Alihosseini, A. Jafari, The effect of porous medium configuration on nanofluid heat transfer, Appl. Nanosci. 10 (2020) 895–906, https://doi.org/10.1007/s13204-019-01192-1.

[21] Q. Li, P. Hu, International Journal of Heat and Mass Transfer Analytical Solutions of Fluid Flow and Heat Transfer in a Partial Porous Channel with Stress Jump and Continuity Interface Conditions Using LTNE Model 128 (2019) 1280–1295, https://doi.org/10.1016/j.ijheatmasstransfer.2018.08.132.

[22] P. Forooghi, M. Abkar, M. Saffar-Avval, Steady and Unsteady Heat Transfer in a Channel Partially Filled with Porous Media Under Thermal Non-Equilibrium Condition, Transp. Porous Media. 86 (2011) 177–198, https://doi.org/10.1007/s11242-010-9615-7.

[23] K.M. Lisboa, Z.Z. José Luiz, R.M. and Cotta,, Hybrid solutions for thermally developing flows in channels partially filled with porous media, Numer. Heat Transf. Part B Fundam. 79 (2021) 189–215, https://doi.org/10.1080/10407790.2020.1819700.

[24] A. Allio, R. Difonzo, A. Leggieri, F. Legrand, R. Marchesin, L. Savoldi, Test and Modeling of the Hydraulic Performance of High-Efficiency Cooling Configurations for Gyrotron Resonance Cavities, Energies 13 (2020), https://doi.org/10.3390/en13051163.

[25] L. Savoldi, A. Allio, A. Bovento, M. Cantone, J. Fernandez Reche, Experimental and numerical investigation of a porous receiver equipped with Raschig Rings for CSP applications, Sol. Energy. (2020).

[26] H. Ebadi, A. Allio, A. Cammi, L. Savoldi, First numerical evaluation of the thermal performance of a tubular receiver equipped with Raschig rings for CSP applications, in: Power 2021, ASME, Virtual, Online, 2021. https://doi.org/10.1115/POWER2021-65714.

[27] H. Ebadi, A. Cammi, R. Difonzo, J. Rodríguez, L. Savoldi, Experimental investigation on an air tubular absorber enhanced with Raschig Rings porous medium in a solar furnace, Appl. Energy. 342 (2023) 30, https://doi.org/10.1016/j.apenergy.2023.121189.

[28] H. Ebadi, A. Cammi, E. Gajetti, L. Savoldi, Development, verification and experimental validation of a 3D numerical model for tubular solar receivers equipped with Raschig Ring porous inserts, Sol. Energy. 267 (2024) 112236, https://doi.org/10.1016/j.solener.2023.112236.

[29] H. Ebadi, A. Cammi, R. Difonzo, J. Rodríguez, L. Savoldi, Experimental investigation on an air tubular absorber enhanced with Raschig Rings porous medium in a solar furnace, Appl. Energy. 342 (2023) 121189.

[30] C.K. Ho, A.R. Mahoney, A. Ambrosini, M. Bencomo, A. Hall, T.N. Lambert, Characterization of Pyromark 2500 for High-Temperature Solar Receivers, (2012) 509–518. https://doi.org/10.1115/ES2012-91374.

[31] S.T. Sileshi, A.A. Hassen, K.D. Adem, Simulation of mixed-mode solar dryer with vertical air distribution channel, Heliyon. 8 (2022) e11898, https://doi.org/10.1016/j.heliyon.2022.e11898.

[32] S.P.S. Inc, Siemens Digital Industries SoftwareSimcenter STAR-CCM + User Guide v2021.1, Siemens (2021).

[33] M.A. Alzoubi, A.P. Sasmito, Thermal performance optimization of a bayonet tube heat exchanger, Appl. Therm. Eng. 111 (2017) 232–247, https://doi.org/10.1016/j.applthermaleng.2016.09.052.

[34] W. Al-Aloosi, Y. Alaiwi, H. Hamzah, Thermal performance analysis in a parabolic trough solar collector with a novel design of inserted fins, Case Stud. Therm. Eng. 49 (2023) 103378, https://doi.org/10.1016/j.csite.2023.103378.

[35] B.S. Petukhov, Heat Transfer and Friction in Turbulent Pipe Flow with Variable Physical Properties, in: J.P. Hartnett, T.F.B.T.-A. in H.T. Irvine (Eds.), Elsevier, 1970: pp. 503–564. https://doi.org/https://doi.org/10.1016/S0065-2717(08)70153-9.

[36] Effect of Input Parameter Uncertainty on Simulation Uncertainty, in: Stand, ASME, Verif. Cation Valid. Comput. Fluid Dyn. Heat Transf., 2009, pp. 1–26.

[37] B. Li, F.A.C. Oliveira, J. Rodríguez, J.C. Fernandes, L.G. Rosa, Numerical and experimental study on improving temperature uniformity of solar furnaces for materials processing, Sol. Energy. 115 (2015) 95–108, https://doi.org/10.1016/j.solener.2015.02.023.

[38] M.I. Roldán, R. Monterreal, Heat flux and temperature prediction on a volumetric receiver installed in a solar furnace, Appl. Energy. 120 (2014) 65–74, https://doi.org/10.1016/j.apenergy.2014.01.029.

[39] M. Wirz, J. Petit, A. Haselbacher, A. Steinfeld, Potential improvements in the optical and thermal efficiencies of parabolic trough concentrators, Sol. Energy. 107 (2014) 398–414. https://doi.org/ 10.1016/j.solener.2014.05.002.

[40] T.T. Zhu, Y.H. Diao, Y.H. Zhao, T.Y. Wang, J. Liu, A Comparative Investigation of Two Types of MHPA Flat-Plate Solar Air Collector Based on Exergy Analysis, J. Sol. Energy Eng. 139 (2017) 1–11, https://doi.org/10.1115/1.4037385.

[41] G. Raam Dheep, A. Sreekumar, Experimental Studies on Energy and Exergy Analysis of a Single-Pass Parallel Flow Solar Air Heater, J. Sol. Energy Eng. 142 (2019), https://doi.org/10.1115/1.4044127.

[42] J. Zhu, K. Wang, G. Li, H. Wu, Z. Jiang, F. Lin, Y. Li, Experimental study of the energy and exergy performance for a pressurized volumetric solar receiver, Appl. Therm. Eng. 104 (2016) 212–221, https://doi.org/10.1016/j.applthermaleng.2016.05.075.

[43] R. Petela, Exergy of undiluted thermal radiation, Sol. Energy. 74 (2003) 469–488, https://doi.org/10.1016/S0038-092X(03)00226-3.

[44] M. Hedayatizadeh, F. Sarhaddi, A. Safavinejad, F. Ranjbar, H. Chaji, Exergy loss-based efficiency optimization of a double-pass/glazed v-corrugated plate solar air heater, Energy 94 (2016) 799–810, https://doi.org/10.1016/j.energy.2015.11.046.

[45] S. Farahat, F. Sarhaddi, H. Ajam, Exergetic optimization of flat plate solar collectors, Renew. Energy. 34 (2009) 1169–1174, https://doi.org/10.1016/j.renene.2008.06.014.

[46] M.M. Matheswaran, T.V. Arjunan, D. Somasundaram, Analytical investigation of solar air heater with jet impingement using energy and exergy analysis, Sol. Energy. 161 (2018) 25–37, https://doi.org/10.1016/j.solener.2017.12.036.

[47] S. Chamoli, N.S. Thakur, Exergetic performance evaluation of solar air heater having V-down perforated baffles on the absorber plate, J. Therm. Anal. Calorim. 117 (2014) 909–923, https://doi.org/10.1007/s10973-014-3765-8.

[48] E. Bellos, I. Daniil, C. Tzivanidis, A Cylindrical Insert for Parabolic Trough Solar Collector 29 (2019) 1846–1876, https://doi.org/10.1108/HFF-05-2018-0190.

[49] E. Bellos, I. Daniil, C. Tzivanidis, Multiple cylindrical inserts for parabolic trough solar collector, Appl. Therm. Eng. 143 (2018) 80–89, https://doi.org/10.1016/j.applthermaleng.2018.07.086.

[50] M. Jadidi, A. Revell, Y. Mahmoudi, Pore-scale large eddy simulation of turbulent flow and heat transfer over porous media, Appl. Therm. Eng. 215 (2022) 118916, https://doi.org/10.1016/j.applthermaleng.2022.118916.

[51] J. Tan, H. Li, B.R. Noack, On the cavity-actuated supersonic mixing layer downstream a thick splitter plate, Phys. Fluids. 32 (2020) 96102, https://doi.org/10.1063/5.0019299.

[52] K. Anirudh, S. Dhinakaran, On the onset of vortex shedding past a two-dimensional porous square cylinder, J. Wind Eng. Ind. Aerodyn. 179 (2018) 200–214. https://doi.org /10.1016/j.jweia.2018.03.004.